

# Extraction of partonic transverse momentum distributions from semi-inclusive deep inelastic scattering, Drell-Yan scattering, and Z-boson production

Alessandro Bacchetta,<sup>1,2,\*</sup> Filippo Delcarro,<sup>1,2,†</sup> Cristian Pisano,<sup>1,2,‡</sup> Marco Radici,<sup>2,§</sup> and Andrea Signori<sup>3,¶</sup>

<sup>1</sup>*Dipartimento di Fisica, Università di Pavia, via Bassi 6, I-27100 Pavia*

<sup>2</sup>*INFN Sezione di Pavia, via Bassi 6, I-27100 Pavia, Italy*

<sup>3</sup>*Theory Center, Thomas Jefferson National Accelerator Facility,  
12000 Jefferson Avenue, Newport News, VA 23606, USA*

(Dated: Monday 27<sup>th</sup> March, 2017, 20:38)

We present an extraction of unpolarized partonic transverse momentum distributions (TMDs) from a simultaneous fit of available data measured in semi-inclusive deep-inelastic scattering, Drell-Yan scattering, and Z boson production. To connect data at different scales, we use TMD evolution at next-to-leading logarithmic accuracy. The analysis is restricted to the low-transverse-momentum region, with no matching to fixed-order calculations at high transverse momentum. We introduce specific choices to deal with TMD evolution at low scales, of the order of 1 GeV<sup>2</sup>. This could be considered as a first attempt at a global fit of TMDs.

PACS numbers: 13.60.Le, 13.87.Fh, 14.20.Dh

## Contents

<b>I. Introduction</b>	2
<b>II. Formalism</b>	2
A. Semi-inclusive DIS	2
B. Drell-Yan and Z production	4
C. TMDs and their evolution	6
<b>III. Data analysis</b>	8
A. Semi-inclusive DIS data	8
1. HERMES data	9
2. COMPASS data	9
B. Low-energy Drell-Yan data	9
C. Z-boson production data	10
D. The replica method	10
<b>IV. Results</b>	12
A. Agreement between data and theory	13
Semi-inclusive DIS	13
Drell-Yan and Z production	14
B. Transverse momentum dependence at 1 GeV	17
C. Modifications to the default choices	21
<b>V. Conclusions</b>	22
<b>Acknowledgments</b>	23
<b>References</b>	23

---

\*Electronic address: [alessandro.bacchetta@unipv.it](mailto:alessandro.bacchetta@unipv.it)

†Electronic address: [filippo.delcarro@pv.infn.it](mailto:filippo.delcarro@pv.infn.it)

‡Electronic address: [cristian.pisano@unipv.it](mailto:cristian.pisano@unipv.it)

§Electronic address: [marco.radici@pv.infn.it](mailto:marco.radici@pv.infn.it)

¶Electronic address: [asignori@jlab.org](mailto:asignori@jlab.org)

## I. INTRODUCTION

Parton distribution functions describe the internal structure of the nucleon in terms of its elementary constituents (quarks and gluons). They cannot be easily computed from first principles, because they require the ability to carry out Quantum Chromodynamics (QCD) calculations in a nonperturbative regime. Many experimental observables in hard scattering experiments involving hadrons are related to parton distribution functions (PDFs) and fragmentation functions (FFs), in a way that is specified by factorization theorems (see, e.g., Refs. [1, 2]). These theorems also elucidate the universality properties of PDFs and FFs (i.e., the fact that they are the same in different processes) and their evolution equations (i.e., how they get modified by the change in the hard scale of the process). Availability of measurements of different processes in different experiments makes it possible to test the reliability of factorization theorems and extract PDFs and FFs through so-called global fits. On the other side, the knowledge of PDFs and FFs allows us to make predictions for other hard hadronic processes. These general statements apply equally well to standard collinear PDFs and FFs and to transverse-momentum-dependent parton distribution functions (TMD PDFs) and fragmentation functions (TMD FFs). Collinear PDFs describe the distribution of partons integrated over all components of partonic momentum except the one collinear to the parent hadron; hence, collinear PDFs are functions of the parton longitudinal momentum fraction  $x$ . TMD PDFs (or TMDs for short) include also the dependence on the transverse momentum  $\mathbf{k}_\perp$ . They can be interpreted as three-dimensional generalizations of collinear PDFs. Similar arguments apply to collinear FFs and TMD FFs [3].

There are several differences between collinear and TMD distributions. From the formal point of view, factorization theorems for the two types of functions are different, implying also different universality properties and evolution equations [4]. From the experimental point of view, observables related to TMDs require the measurement of some transverse momentum component much smaller than the hard scale of the process [5, 6]. For instance, Deep-Inelastic Scattering (DIS) is characterized by a hard scale represented by the 4-momentum squared of the virtual photon ( $-Q^2$ ). In inclusive DIS this is the only scale of the process, and access is limited to collinear PDFs and FFs. In semi-inclusive DIS (SIDIS) also the transverse momentum of the outgoing hadron ( $P_{hT}$ ) can be measured [7, 8]. If  $P_{hT}^2 \ll Q^2$ , TMD factorization can be applied and the process is sensitive to TMDs [2].

If polarization is taken into account, several TMDs can be introduced [7, 9–12]. Attempts to extract some of them have already been presented in the past [13–21]. In this work, we focus on the simplest ones, i.e., the unpolarized TMD PDF  $f_1^q(x, k_\perp^2)$  and the unpolarized TMD FF  $D_1^{q \rightarrow h}(z, P_\perp^2)$ , where  $z$  is the fractional energy carried by the detected hadron  $h$ ,  $k_\perp$  is the transverse momentum of the parton with respect to the parent hadron, and  $P_\perp$  is the transverse momentum of the produced hadron with respect to the parent parton. Despite their simplicity, the phenomenology of these unpolarized TMDs presents several challenges [22]: the choice of a functional form for the nonperturbative components of TMDs, the inclusion of a possible dependence on partonic flavor [23], the implementation of TMD evolution [4, 24], the matching to fixed-order calculations in collinear factorization [25].

We take into consideration three kinds of processes: SIDIS, and Drell–Yan processes (DY) and the production of  $Z$  bosons. To date, they represent all possible processes where experimental information is available for unpolarized TMD extractions. The only important process currently missing is electron-positron annihilation, which is particularly important for the determination of TMD FFs [24]. This work can therefore be considered as the first attempt at a global fit of TMDs.

The paper is organized as follows. In Sec. II, the general formalism for TMDs in SIDIS, DY processes, and  $Z$  production is briefly outlined, including a description of the assumptions and approximations in the phenomenological implementation of TMD evolution equations. In Sec. III, the criteria for selecting the data analyzed in the fit are summarized and commented. In Sec. IV, the results of our global fit are presented and discussed. In Sec. V, we summarize the results and present an outlook for future analyses.

## II. FORMALISM

### A. Semi-inclusive DIS

In one-particle SIDIS, a lepton  $\ell$  with momentum  $l$  scatters off a hadron target  $N$  with mass  $M$  and momentum  $P$ . In the final state, the scattered lepton momentum  $l'$  is measured together with one hadron  $h$  with mass  $M_h$  and momentum  $P_h$ . The corresponding reaction formula is

$$\ell(l) + N(P) \rightarrow \ell(l') + h(P_h) + X. \quad (1)$$

The space-like momentum transfer is  $q = l - l'$ , with  $Q^2 = -q^2$ . We introduce the usual invariants

$$x = \frac{Q^2}{2P \cdot q}, \quad y = \frac{P \cdot q}{P \cdot l}, \quad z = \frac{P \cdot P_h}{P \cdot q}, \quad \gamma = \frac{2Mx}{Q}. \quad (2)$$

The available data refer to SIDIS hadron multiplicities, namely to the differential number of hadrons produced per corresponding inclusive DIS event. In terms of cross sections, we define the multiplicities as

$$m_N^h(x, z, |\mathbf{P}_{hT}|, Q^2) = \frac{d\sigma_N^h/(dx dz d|\mathbf{P}_{hT}| dQ^2)}{d\sigma_{\text{DIS}}/(dx dQ^2)}, \quad (3)$$

where  $d\sigma_N^h$  is the differential cross section for the SIDIS process and  $d\sigma_{\text{DIS}}$  is the corresponding inclusive one, and where  $\mathbf{P}_{hT}$  is the component of  $\mathbf{P}_h$  transverse to  $\mathbf{q}$  (we follow here the notation suggested in Ref. [26]). In the single-photon-exchange approximation, the multiplicities can be written as ratios of structure functions (see [8] for details):

$$m_N^h(x, z, |\mathbf{P}_{hT}|, Q^2) = \frac{2\pi |\mathbf{P}_{hT}| F_{UU,T}(x, z, \mathbf{P}_{hT}^2, Q^2) + 2\pi \varepsilon |\mathbf{P}_{hT}| F_{UU,L}(x, z, \mathbf{P}_{hT}^2, Q^2)}{F_T(x, Q^2) + \varepsilon F_L(x, Q^2)}, \quad (4)$$

where

$$\varepsilon = \frac{1 - y - \frac{1}{4}\gamma^2 y^2}{1 - y + \frac{1}{2}y^2 + \frac{1}{4}\gamma^2 y^2}. \quad (5)$$

The structure function  $F_{XY,Z}$  corresponds to a lepton with polarization  $X$  scattering on a target with polarization  $Y$  by exchanging a virtual photon in a polarization state  $Z$ .

The semi-inclusive cross section can be expressed in a factorized form in terms of TMDs only in the kinematic limits  $M^2 \ll Q^2$  and  $\mathbf{P}_{hT}^2 \ll Q^2$ . In these limits, the structure function  $F_{UU,L}$  of Eq. (4) can be neglected [27]. The structure function  $F_L$  in the denominator contains contributions involving powers of the strong coupling constant  $\alpha_S$  at an order that goes beyond the level reached in this analysis; hence, it will be consistently neglected (for measurements and estimates of the  $F_L$  structure function see, e.g., Refs. [28, 29] and references therein).

To express the structure functions in terms of TMD PDFs and FFs, we rely on the factorized formula for SIDIS [2, 30–37] (see Fig. 1 for a graphical representation of the involved transverse momenta):

$$\begin{aligned} F_{UU,T}(x, z, \mathbf{P}_{hT}^2, Q^2) &= \sum_a \mathcal{H}_{UU,T}^a(Q^2) \\ &\times x \int d^2 \mathbf{k}_\perp d^2 \mathbf{P}_\perp f_1^a(x, \mathbf{k}_\perp^2; Q^2) D_1^{a \rightarrow h}(z, \mathbf{P}_\perp^2; Q^2) \delta^{(2)}(z \mathbf{k}_\perp - \mathbf{P}_{hT} + \mathbf{P}_\perp) \\ &+ Y_{UU,T}(Q^2, \mathbf{P}_{hT}^2) + \mathcal{O}(M^2/Q^2). \end{aligned} \quad (6)$$

Here,  $\mathcal{H}_{UU,T}$  is the hard scattering part;  $f_1^a(x, \mathbf{k}_\perp^2; Q^2)$  is the TMD distribution of unpolarized partons with flavor  $a$  in an unpolarized proton, carrying longitudinal momentum fraction  $x$  and transverse momentum  $\mathbf{k}_\perp$ . The  $D_1^{a \rightarrow h}(z, \mathbf{P}_\perp^2; Q^2)$  is the TMD fragmentation function describing the fragmentation of an unpolarized parton with flavor  $a$  into an unpolarized hadron  $h$  carrying longitudinal momentum fraction  $z$  and transverse momentum  $\mathbf{P}_\perp$ . TMDs generally depend on two energy scales [2]: the first enters via the renormalization group evolution, whereas the second is associated to the rapidity renormalization and enters via a process-independent soft factor. In this work we choose them to be equal and set to  $Q^2$ . The term  $Y_{UU,T}$  is introduced to ensure a matching to the perturbative fixed-order calculations at higher transverse momenta.

In our analysis, we neglect any correction of the order of  $M^2/Q^2$  or higher to Eq. (6). At large  $Q^2$  this is well justified. However, fixed-target DIS experiments typically collect a large amount of data at relatively low  $Q^2$  values, where these assumptions should be all tested in future studies. The reliability of the theoretical description of SIDIS at low  $Q^2$  has been recently discussed in Refs. [39, 40].

Eq. (6) can be expanded in powers of  $\alpha_S$ . In the present analysis, we will consider only the leading order terms in  $\alpha_S$ , i.e., stop at order  $\alpha_S^0$ . In this case  $\mathcal{H}_{UU,T}^a(Q^2) \approx e_a^2$  and  $Y_{UU,T} \approx 0$ . However, perturbative corrections include large logarithms  $L \equiv \log(z^2 Q^2 / P_{hT}^2)$ , so that  $\alpha_S L \approx 1$ . In the present analysis, we will take into account all leading and Next-to-Leading Logarithms (NLL).<sup>1</sup>

---

<sup>1</sup> We remark that formulas at NNLL are available in the literature [41].

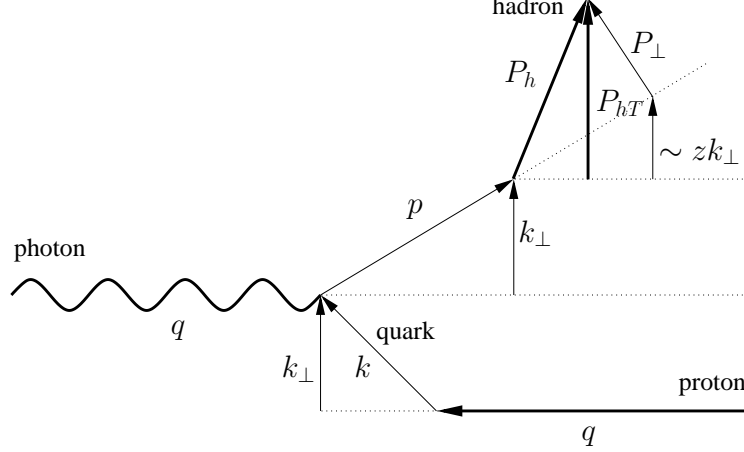


FIG. 1: Diagram describing the relevant momenta involved in a semi-inclusive DIS event (see also Ref. [38]): a virtual photon (defining the reference axis) strikes a parton inside a proton. The parton has a transverse momentum  $\mathbf{k}_\perp$  (not measured). The struck parton fragments into a hadron, which acquires a further transverse momentum  $\mathbf{P}_\perp$  (not measured). The total measured transverse-momentum of the final hadron is  $\mathbf{P}_{hT}$ . When  $Q^2$  is very large, the longitudinal components are all much larger than the transverse components. In this regime,  $\mathbf{P}_{hT} \approx z\mathbf{k}_\perp + \mathbf{P}_\perp$ .

In these approximations (LO in  $\alpha_S$  and NLL), only the first term in Eq. (6) is relevant (often in the literature this has been called  $W$  term). We expect this term to provide a good description of the structure function only in the region where  $P_{hT}^2 \ll Q^2$ . It can happen that  $Y_{UU,T}$ , defined in the standard way (see, e.g., Ref. [31]), gives large contributions also in this region, but it is admissible to redefine it in order to avoid this problem [25]. We leave a detailed treatment of the matching to the high  $P_{hT}^2 \approx Q^2$  region to future investigations.

To the purpose of applying TMD evolution equations, we need to calculate the Fourier transform of the the part of Eq. (6) involving TMDs. The structure function thus reduces to

$$F_{UU,T}(x, z, \mathbf{P}_{hT}^2, Q^2) \approx 2\pi \sum_a e_a^2 x \int_0^\infty d\xi_T \xi_T J_0(\xi_T |\mathbf{P}_{hT}|/z) \tilde{f}_1^a(x, \xi_T^2; Q^2) \tilde{D}_1^{a-h}(z, \xi_T^2; Q^2).$$

where we introduced the Fourier transforms of the TMD PDF and FF according to

$$\tilde{f}_1^a(x, \xi_T^2; Q^2) = \int_0^\infty d|\mathbf{k}_\perp| |\mathbf{k}_\perp| J_0(\xi_T |\mathbf{k}_\perp|) f_1^a(x, \mathbf{k}_\perp^2; Q^2), \quad (7)$$

$$\tilde{D}_1^{a-h}(z, \xi_T^2; Q^2) = \int_0^\infty \frac{d|\mathbf{P}_\perp|}{z^2} |\mathbf{P}_\perp| J_0(\xi_T |\mathbf{P}_\perp|/z) D_1^{a-h}(z, \mathbf{P}_\perp^2; Q^2). \quad (8)$$

## B. Drell–Yan and Z production

In a Drell–Yan process, two hadrons  $A$  and  $B$  with momenta  $P_A$  and  $P_B$  collide at a center-of-mass energy squared  $s = (P_A + P_B)^2$  and produce a virtual photon or a  $Z$  boson plus hadrons. The boson decays into a lepton-antilepton pair. The reaction formula is

$$A(P_A) + B(P_B) \rightarrow [\gamma^*/Z + X \rightarrow] \ell^+(l) + \ell^-(l') + X. \quad (9)$$

The invariant mass of the virtual photon is  $Q^2 = q^2$  with  $q = l + l'$ . We introduce the rapidity of the virtual photon/ $Z$  boson

$$\eta = \frac{1}{2} \log \left( \frac{q^0 + q_z}{q^0 - q_z} \right). \quad (10)$$

where the  $z$  direction is defined along the momentum of hadron  $A$ .

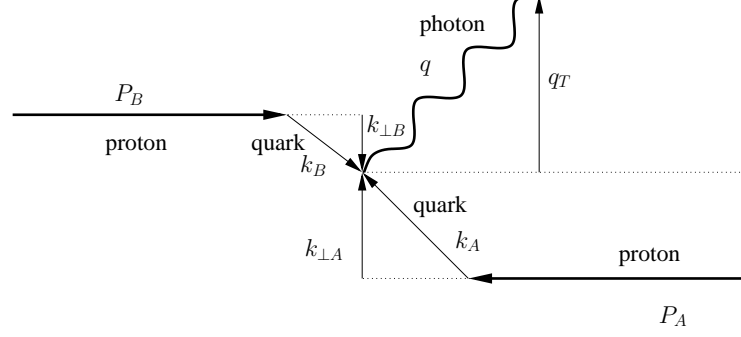


FIG. 2: Diagram describing the relevant momenta involved in a Drell-Yan event: two partons from two hadrons collide. They have transverse momenta  $\mathbf{k}_{\perp A}$  and  $\mathbf{k}_{\perp B}$  (not measured). They produce a virtual photon with (measured) transverse momentum  $\mathbf{q}_T = \mathbf{k}_{\perp A} + \mathbf{k}_{\perp B}$  with respect to the hadron collision axis.

The cross section can be written in terms of structure functions [42, 43]. For our purposes, we need the unpolarized cross section integrated over  $d\Omega$  and over the azimuthal angle of the virtual photon,

$$\frac{d\sigma}{dQ^2 dq_T^2 d\eta} = \sigma_0^{\gamma, Z} \left( F_{UU}^1 + \frac{1}{2} F_{UU}^2 \right). \quad (11)$$

The elementary cross sections are

$$\sigma_0^\gamma = \frac{4\pi^2 \alpha_{\text{em}}^2}{3Q^2 s}, \quad \sigma_0^Z = \frac{\pi^2 \alpha_{\text{em}}}{s \sin^2 \theta_W \cos^2 \theta_W} B_R(Z \rightarrow \ell^+ \ell^-) \delta(Q^2 - M_Z^2), \quad (12)$$

where  $\theta_W$  is Weinberg's angle,  $M_Z$  is the mass of the  $Z$  boson, and  $B_R(Z \rightarrow \ell^+ \ell^-)$  is the branching ratio for the  $Z$  boson decay in two leptons. We adopted the narrow-width approximation, i.e., we neglect contributions for  $Q^2 \neq M_Z^2$ . We used the values  $\sin^2 \theta_W = 0.2313$ ,  $M_Z = 91.18$  GeV, and  $B_R(Z \rightarrow \ell^+ \ell^-) = 3.366$  [44]. Similarly to the SIDIS case, in the kinematic limit  $q_T^2 \ll Q^2$  the structure function  $F_{UU}^2$  can be neglected (for measurement and estimates of this structure function see, e.g., Ref. [45] and references therein).

The longitudinal momentum fractions of the annihilating quarks can be written in terms of rapidity in the following way

$$x_A = \frac{Q}{\sqrt{s}} e^\eta, \quad x_B = \frac{Q}{\sqrt{s}} e^{-\eta}. \quad (13)$$

Some experiments use the variable  $x_F$ , which is connected to the other variables by the following relations

$$\eta = \sinh^{-1} \left( \frac{\sqrt{s}}{Q} \frac{x_F}{2} \right), \quad x_A = \sqrt{\frac{Q^2}{s} + \frac{x_F^2}{4}} + \frac{x_F}{2}, \quad x_B = x_A - x_F. \quad (14)$$

The structure function  $F_{UU}^1$  can be written as (see Fig. 2 for a graphical representation of the involved transverse momenta)

$$\begin{aligned} F_{UU}^1(x_A, x_B, \mathbf{q}_T^2, Q^2) &= \sum_a \mathcal{H}_{UU}^{1a}(Q^2) \\ &\times x_A x_B \int d^2 \mathbf{k}_{\perp A} d^2 \mathbf{k}_{\perp B} f_1^a(x_A, \mathbf{k}_{\perp A}^2; Q^2) f_1^{\bar{a}}(x_B, \mathbf{k}_{\perp B}^2; Q^2) \delta^{(2)}(\mathbf{k}_{\perp A} - \mathbf{q}_T + \mathbf{k}_{\perp B}) \\ &+ Y_{UU}^1(Q^2, \mathbf{q}_T^2) + \mathcal{O}(M^2/Q^2). \end{aligned} \quad (15)$$

As in the SIDIS case, in our analysis we neglect the  $Y_{UU}$  term and we consider the hard coefficients only up to leading order in the couplings, i.e.,

$$\mathcal{H}_{UU, \gamma}^{1a}(Q^2) \approx \frac{e_a^2}{N_c}, \quad \mathcal{H}_{UU, Z}^{1a}(Q^2) \approx \frac{V_a^2 + A_a^2}{N_c}, \quad (16)$$

where<sup>2</sup>

$$V_a = I_{3a} - 2e_a \sin \theta_W , \quad A_a = I_{3a} . \quad (17)$$

The structure function can be conveniently expressed as a Fourier transform of the right-hand side of Eq. (15) as

$$F_{UU}^1(x_A, x_B, \mathbf{q}_T^2, Q^2) \approx 2\pi \sum_a \mathcal{H}_{UU}^{1a} x_a x_B \int_0^\infty d\xi_T \xi_T J_0(\xi_T |\mathbf{q}_T|) \tilde{f}_1^a(x_A, \xi_T^2; Q^2) \tilde{f}_1^a(x_B, \xi_T^2; Q^2) . \quad (18)$$

### C. TMDs and their evolution

Evolution equations quantitatively describe the connection between different values for the energy scales. In the following we will set their initial values to  $\mu_b^2$  and their final values as  $Q^2$ , so that only  $Q^2$  and  $\mu_b^2$  need to be specified in a TMD distribution. Following the formalism of Refs. [2, 34], the unpolarized TMD distribution and fragmentation functions in configuration space for a parton flavor  $a$  at a certain scale  $Q^2$  can be written as

$$\tilde{f}_1^a(x, \xi_T^2; Q^2) = \sum_{i=q, \bar{q}, g} (C_{a/i} \otimes f_1^i)(x, \bar{\xi}_*, \mu_b^2) e^{S(\mu_b^2, Q^2)} \left( \frac{Q^2}{\mu_b^2} \right)^{-K(\bar{\xi}_*; \mu_b)} \left( \frac{Q^2}{Q_0^2} \right)^{g_K(\xi_T)} \tilde{f}_{\text{1NP}}^a(x, \xi_T^2) , \quad (19)$$

$$\tilde{D}_1^{a \rightarrow h}(z, \xi_T^2; Q^2) = \sum_{i=q, \bar{q}, g} (\hat{C}_{a/i} \otimes D_1^{i \rightarrow h})(z, \bar{\xi}_*, \mu_b^2) e^{S(\mu_b^2, Q^2)} \left( \frac{Q^2}{\mu_b^2} \right)^{-K(\bar{\xi}_*; \mu_b)} \left( \frac{Q^2}{Q_0^2} \right)^{g_K(\xi_T)} \tilde{D}_{\text{1NP}}^{a \rightarrow h}(z, \xi_T^2) . \quad (20)$$

The collinear distributions in Eqs. (27), (28) and the perturbative Sudakov form factor  $S$  involve the scale  $\mu_b^2$ . We choose it to be

$$\mu_b = \frac{2e^{-\gamma_E}}{\bar{\xi}_*} , \quad (21)$$

where  $\gamma_E$  is the Euler constant and

$$\bar{\xi}_* \equiv \bar{\xi}_*(\xi_T; \xi_{\min}, \xi_{\max}) = \xi_{\max} \left( \frac{1 - e^{-\xi_T^4/\xi_{\max}^4}}{1 - e^{-\xi_T^4/\xi_{\min}^4}} \right)^{1/4} . \quad (22)$$

This variable replaces the simple dependence upon  $\xi_T$  in the convolutions of Eqs. (19), (20) (see also Eqs. (24), (25) later) and in the perturbative Sudakov factor  $S$ ; namely, in the perturbative parts of the TMD definitions of Eqs. (19), (20). In fact, at large  $\xi_T$  these parts are no longer reliable. Therefore, the  $\bar{\xi}_*$  is chosen to saturate on the maximum value  $\xi_{\max}$ , as suggested by the CSS formalism [2, 34]. On the other hand, at small  $\xi_T$  the TMD formalism is not valid and should be matched to the fixed-order collinear calculations. The way the matching is implemented is arbitrary. In any case, the TMD contribution can be arbitrarily modified at small  $\xi_T$ . In our approach, we choose to saturate  $\bar{\xi}_*$  at the minimum value  $\xi_{\min} \propto 1/Q$ . With the appropriate choices, for  $\xi_T = 0$  the Sudakov exponent vanishes, as it should [46, 47]. Our choice partially corresponds to modifying the resummed logarithms as in Ref. [48] and to other similar modifications proposed in the literature [25, 49]. One advantage of these kind of prescriptions is that by integrating over the impact parameter  $\xi_T$ , the collinear expression for the cross section in terms of collinear PDFs is recovered, at least at leading order [25]. We remind the reader that there are different schemes available to deal with the high- $\xi_T$  region, such as the so-called “complex- $\xi$  prescription” [50] or an extrapolation of the perturbative small- $\xi_T$  calculation to the large  $\xi_T$  region based on dynamical power corrections [51].

The values of  $\xi_{\max}$  and  $\xi_{\min}$  could be regarded as arbitrary scales separating perturbative from nonperturbative regimes. We choose to fix them to the values

$$\xi_{\max} = 2e^{-\gamma_E} \text{ GeV}^{-1} \approx 1.123 \text{ GeV}^{-1}, \quad \xi_{\min} = 2e^{-\gamma_E}/Q . \quad (23)$$

The motivations are the following:

---

<sup>2</sup> We remind the reader that the value of weak isospin  $I_3$  is equal to +1 for  $u, c, t$  and -1 for  $d, s, b$ .

- with the above choices, the scale  $\mu_b$  is constrained between 1 GeV and  $Q$ , so that the collinear PDFs are never computed at a scale lower than 1 GeV and the lower limit of the integrals contained in the definition of the perturbative Sudakov factor (see Eq. (29)) can never become larger than the upper limit;
- at  $Q = Q_0 = 1$  GeV,  $\xi_{\max} = \xi_{\min}$  and there are no evolution effects; the TMD is simply given by the corresponding collinear function multiplied by a nonperturbative contribution depending on  $k_\perp$  (plus possible corrections of order  $\alpha_S$  from the Wilson coefficients).

The Collins-Soper kernel  $K$  is a power series in  $\alpha_S$  with coefficients involving  $\ln \mu/\mu_b$ . At NLL accuracy,  $K(\bar{\xi}_*, \mu_b) = 0$ . Similarly, the  $C$  and  $\hat{C}$  are perturbatively calculable Wilson coefficients for the TMD distribution and fragmentation functions, respectively. They are convoluted with the corresponding collinear functions according to

$$(C_{a/i} \otimes f_1^i)(x, \bar{\xi}_*, \mu_b^2) = \int_x^1 \frac{du}{u} C_{a/i}\left(\frac{x}{u}, \bar{\xi}_*, \alpha_S(\mu_b^2)\right) f_1^i(u; \mu_b^2), \quad (24)$$

$$(\hat{C}_{a/i} \otimes D_1^{i \rightarrow h})(z, \bar{\xi}_*, \mu_b^2) = \int_z^1 \frac{du}{u} \hat{C}_{a/i}\left(\frac{z}{u}, \bar{\xi}_*, \alpha_S(\mu_b^2)\right) D_1^{i \rightarrow h}(u; \mu_b^2). \quad (25)$$

In the present analysis, we consider only the leading-order term in the  $\alpha_S$  expansion for  $C$ ,  $\hat{C}$ , i.e.,

$$C_{a/i}\left(\frac{x}{u}, \bar{\xi}_*, \alpha_S(\mu_b^2)\right) \approx \delta_{ai} \delta(1 - x/u), \quad \hat{C}_{a/i}\left(\frac{z}{u}, \bar{\xi}_*, \alpha_S(\mu_b^2)\right) \approx \delta_{ai} \delta(1 - z/u). \quad (26)$$

As a consequence of the choices we made, the expression for the evolved TMD functions reduces to

$$\tilde{f}_1^a(x, \xi_T^2; Q^2) = f_1^a(x; \mu_b^2) e^{S(\mu_b^2, Q^2)} e^{g_K(\xi_T) \ln(Q^2/Q_0^2)} \tilde{f}_{\text{INP}}^a(x, \xi_T^2), \quad (27)$$

$$\tilde{D}_1^{a \rightarrow h}(z, \xi_T^2; Q^2) = D_1^{a \rightarrow h}(z; \mu_b^2) e^{S(\mu_b^2, Q^2)} e^{g_K(\xi_T) \ln(Q^2/Q_0^2)} \tilde{D}_{\text{INP}}^{a \rightarrow h}(z, \xi_T^2). \quad (28)$$

The Sudakov exponent  $S$  can be written as

$$S(\mu_b^2, Q^2) = - \int_{\mu_b^2}^{Q^2} \frac{d\mu^2}{\mu^2} \left[ A(\alpha_S(\mu^2)) \ln\left(\frac{Q^2}{\mu^2}\right) + B(\alpha_S(\mu^2)) \right], \quad (29)$$

where the functions  $A$  and  $B$  have a perturbative expansions of the form

$$A(\alpha_S(\mu^2)) = \sum_{k=1}^{\infty} A_k \left( \frac{\alpha_S}{\pi} \right)^k, \quad B(\alpha_S(\mu^2)) = \sum_{k=1}^{\infty} B_k \left( \frac{\alpha_S}{\pi} \right)^k. \quad (30)$$

To NNLL accuracy, we need the following terms [31, 52]

$$A_1 = C_F, \quad A_2 = \frac{1}{2} C_F \left[ C_A \left( \frac{67}{18} - \frac{\pi^2}{6} \right) - \frac{5}{9} N_f \right], \quad B_1 = -\frac{3}{2} C_F. \quad (31)$$

We use the approximate analytic expression for  $\alpha_S$  at NLO with the  $\Lambda_{\text{QCD}} = 340$  MeV, 296 MeV, 214 MeV for three, four, five flavors, respectively, corresponding to a value of  $\alpha_S(M_Z) = 0.117$ . We fix the flavor thresholds at  $m_c = 1.5$  GeV and  $m_b = 4.7$  GeV. The integration of the Sudakov exponent in Eq. (29) can be done analytically (for the complete expressions see, e.g., Refs. [36, 53, 54]).

Following Refs. [55–57], for the nonperturbative Sudakov factor we make the traditional choice

$$g_K(\xi_T) = -g_2 \xi_T^2 / 2 \quad (32)$$

with  $g_2$  a free parameter. Recently, several alternative forms have been proposed [58, 59]. Also, recent theoretical studies aimed at calculating this term using nonperturbative methods [60]. All these choices should be tested in future studies. In Ref. [61], a good agreement with data was achieved even without this term: **we think (anche gli autori della ref. stessa lo dicono)** this is not possible when including data at low  $Q^2$ .

In this analysis, for the collinear PDFs  $f_1^a$  we adopt the GJR08FFnLO set [62] through the LHAPDF library [63], and for the collinear fragmentation functions the DSS14 NLO set for pions [64] and the DSS07 NLO set for kaons [65].<sup>3</sup> We will comment on the use of other PDF sets in Sec. IV C.

<sup>3</sup> After the completion of our analysis, a new set of kaon fragmentation function was presented in Ref. [66].

We parametrize the intrinsic nonperturbative parts of the TMDs in the following ways

$$\tilde{f}_{\text{1NP}}^a(x, \xi_T^2) = \frac{1}{2\pi} e^{-g_{1a} \frac{\xi_T^2}{4}} \left( 1 - \frac{\lambda g_{1a}^2}{1 + \lambda g_{1a}} \frac{\xi_T^2}{4} \right), \quad (33)$$

$$\tilde{D}_{\text{1NP}}^{a \rightarrow h}(z, \xi_T^2) = \frac{g_{3a \rightarrow h} e^{-g_{3a \rightarrow h} \frac{\xi_T^2}{4z^2}} + (\lambda_F/z^2) g_{4a \rightarrow h}^2 \left( 1 - g_{4a \rightarrow h} \frac{\xi_T^2}{4z^2} \right) e^{-g_{4a \rightarrow h}^2 \frac{\xi_T^2}{4z^2}}}{2\pi z^2 \left( g_{3a \rightarrow h} + (\lambda_F/z^2) g_{4a \rightarrow h}^2 \right)}. \quad (34)$$

After performing the anti-Fourier transform, the  $f_{\text{1NP}}$  and  $D_{\text{1NP}}$  in momentum space correspond to the normalized linear combination of a Gaussian and a weighted Gaussian:

$$f_{\text{1NP}}^a(x, \mathbf{k}_\perp^2) = \frac{1}{\pi} \frac{(1 + \lambda \mathbf{k}_\perp^2)}{g_{1a} + \lambda g_{1a}^2} e^{-\frac{\mathbf{k}_\perp^2}{g_{1a}}}, \quad (35)$$

$$D_{\text{1NP}}^{a \rightarrow h}(z, \mathbf{P}_\perp^2) = \frac{1}{\pi} \frac{1}{g_{3a \rightarrow h} + (\lambda_F/z^2) g_{4a \rightarrow h}^2} \left( e^{-\frac{\mathbf{P}_\perp^2}{g_{3a \rightarrow h}}} + \lambda_F \frac{\mathbf{P}_\perp^2}{z^2} e^{-\frac{\mathbf{P}_\perp^2}{g_{4a \rightarrow h}}} \right). \quad (36)$$

In the TMD PDF case, the Gaussian and the weighted Gaussian have the same width, while in the fragmentation function, we considered the possibility that the two Gaussian widths are different. The choice of this particular functional form is motivated by model calculations: the weighted Gaussian could arise from the presence of components of the quark wave function with angular momentum  $L = 1$  [67–71].

The Gaussian width of the TMD distributions may depend on the parton flavor  $a$  [23]. In the present analysis, however, we assume they are flavor independent. The justification for this choice is that most of the data we are considering are not sufficiently sensitive to flavor differences.

Finally, we assume that the Gaussian width of the TMD depends on fractional longitudinal momentum  $x$  according to

$$g_1(x) = N_1 \frac{(1-x)^\alpha x^\sigma}{(1-\hat{x})^\alpha \hat{x}^\sigma}, \quad (37)$$

where  $\alpha$ ,  $\sigma$ , and  $N_1 \equiv g_1(\hat{x})$  with  $\hat{x} = 0.1$ , are free parameters. Similarly, for fragmentation functions we have

$$g_{3,4}(z) = N_{3,4} \frac{(z^\beta + \delta) (1-z)^\gamma}{(\hat{z}^\beta + \delta) (1-\hat{z})^\gamma}, \quad (38)$$

where  $\beta$ ,  $\gamma$ ,  $\delta$ , and  $N_{3,4} \equiv g_{3,4}(\hat{z})$  with  $\hat{z} = 0.5$  are free parameters.

The average transverse momentum squared for the distributions in Eq. (35) and (36) can be computed analytically:

$$\langle \mathbf{k}_\perp^2 \rangle(x) = \frac{g_1(x) + 2\lambda g_1^2(x)}{1 + \lambda g_1(x)}, \quad \langle \mathbf{P}_\perp^2 \rangle(z) = \frac{g_3^2(z) + 2\lambda_F g_4^3(z)}{g_3(z) + \lambda_F g_4^2(z)}. \quad (39)$$

### III. DATA ANALYSIS

The main goals of our work are to extract the magnitude of intrinsic transverse momenta, to study the evolution of TMD parton distributions and fragmentation functions over a large enough range of energy and to test their universality among different processes. To achieve this we included measurements taken from SIDIS, Drell-Yan and  $Z$  boson production from different experimental collaborations at different energy scales. In this chapter we describe the data sets considered for each process and the kinematic cuts applied.

Tab. I refers to the data sets for SIDIS off proton target (HERMES experiment) and presents their kinematic ranges. The same holds for Tab. II, Tab. III, Tab. IV for SIDIS off deuteron (HERMES and COMPASS experiments), Drell-Yan events at low energy and  $Z$  boson production respectively. If not specified otherwise, the theoretical formulas are computed at the average values of the kinematic variables in each bin.

#### A. Semi-inclusive DIS data

The semi-inclusive DIS data are taken from HERMES [72] and COMPASS [73] experiments. Both HERMES and COMPASS data have been already analyzed in previous works, e.g., Refs. [23, 74], however they have never been fitted together, considering also the contributions deriving from TMD evolution.



The application of the TMD formalism to SIDIS depends on the capability of identifying the current fragmentation region. This task has been recently discussed in Ref. [39], where the authors point out a possible overlap among different fragmentation regions when the hard scale  $Q$  is sufficiently low. In this paper we do not tackle this problem and we leave it to future studies. As described in Tabs. I and II, we identify the current fragmentation region operating a cut on  $z$  only, namely  $0.2 < z < 0.74$ .

Another requirement for the applicability of TMD factorization is the presence of two separate scales in the process. In SIDIS, those are the  $Q^2$  and  $P_{hT}^2$ , which should satisfy the condition  $P_{hT}^2 \ll Q^2$ , or more precisely  $P_{hT}^2/z^2 \ll Q^2$ . We implement this condition by imposing  $P_{hT} < \min[0.2 Q, 0.7 Qz] + 0.5 \text{ GeV}$ . With this choice,  $P_{hT}^2$  is always smaller than  $Q^2/3$ , but in a few bins (at low  $Q^2$  and  $z$ )  $P_{hT}^2/z^2$  may become larger than  $Q^2$ . The applicability of TMD factorization in this case could be questioned. However, as we will explain further in Sec. IV C, we can obtain a fit that can describe a wide region of  $P_{hT}$  and can also perform very well in a restricted region, where TMD factorization certainly holds.

All these choices are summarized in Tabs. I and II.

### 1. HERMES data

HERMES hadron multiplicities are measured in a fixed target experiment, colliding a 27.6 GeV lepton beam on a hydrogen ( $p$ ) or deuterium ( $D$ ) gas target, for a total of 2688 points. These are grouped in bins of  $(x, z, Q^2, P_{hT})$  with the average values of  $(x, Q^2)$  ranging from about  $(0.04, 1.25 \text{ GeV}^2)$  to  $(0.4, 9.2 \text{ GeV}^2)$ . The collinear energy fraction  $z$  in Eq. (2) ranges in  $0.1 \leq z \leq 0.9$ . The transverse momentum of the detected hadron satisfies  $0.1 \text{ GeV} \leq |P_{hT}| \leq 1.3 \text{ GeV}$ . The peculiarity of HERMES SIDIS experiment lies in the ability of its detector to distinguish between pions and kaons in the final state, in addition to determining their momenta and charges. The particle identification process distinguish the final data sets in eight different channels, one for every combination of target ( $p, D$ ) and detected charged hadron ( $\pi^\pm, K^\pm$ ). The HERMES collaboration published two distinct sets, characterized by the inclusion or subtraction of the vector meson contribution. In our work we considered only the data set where these contributions have been subtracted.

### 2. COMPASS data

The COMPASS collaboration extracted multiplicities for charge-separated but unidentified hadrons produced in SIDIS off a deuteron ( $^6\text{LiD}$ ) target [73]. The number of data is an order of magnitude higher compared to the HERMES experiment. The data are organized in multidimensional bins of  $(x, z, Q^2, P_{hT})$ , they cover a range in  $(x, Q^2)$  from about  $(0.005, 1.11 \text{ GeV}^2)$  to  $(0.09, 7.57 \text{ GeV}^2)$  and the interval  $0.2 \leq z \leq 0.8$ . Similarly to HERMES, for COMPASS  $P_{hT}^2 \lesssim 1 \text{ GeV}^2$ . The multiplicities published by COMPASS are affected by normalization errors (see the *erratum* to Ref. [73]). In order to avoid this issue, we divide the data in each bin in  $(x, z, Q^2)$  by the data point with the lowest  $P_{hT}^2$  in the bin. As a result, we define the *normalized* multiplicity as

$$m_{\text{norm}}(x, z, \mathbf{P}_{hT}^2, Q^2) = \frac{m_N^h(x, z, \mathbf{P}_{hT}^2, Q^2)}{m_N^h(x, z, \min[\mathbf{P}_{hT}^2], Q^2)} , \quad (40)$$

where the multiplicity  $m_N^h$  is defined in Eq. (3). Fitting normalized multiplicities the first data point of each bin is considered as a fixed parameter and excluded from the degrees of freedom of the system.

## B. Low-energy Drell-Yan data

We analyze Drell-Yan events collected by fixed-target experiments at low-energy. These data set have been considered also in previous works, e.g., in Ref. [56, 57, 75, 76]. We used data sets from the E288 experiment [77], that measured the invariant dimuon cross section  $Ed^3\sigma/dq^3$  for the production of  $\mu^+\mu^-$  pairs from the collision of a proton beam with a fixed target, either composed of Cu or Pt. The measurements were repeated using proton incident energies of 200, 300 and 400 GeV, producing three different data sets. Their respective center of mass energies are  $\sqrt{s} = 19.4, 23.8, 27.4 \text{ GeV}$ . We also included the set of measurements  $Ed^3\sigma/dq^3$  from E605 [78], extracted from the collision of a proton beam with an energy of 800 GeV ( $\sqrt{s} = 38.8 \text{ GeV}$ ) on a copper fixed target.

The explored  $Q$  values are higher compared to the SIDIS case, as can be seen in Tab. III. E288 provides data at fixed rapidity, whereas E605 provides data at fixed  $x_F = 0.1$ . As discussed for SIDIS data, we can apply TMD factorization if  $\Lambda_{\text{QCD}}^2 \ll q_T^2 \ll Q^2$ , where  $q_T$  is the transverse momentum of the intermediate electroweak boson,

reconstructed from the kinematics of the final state leptons. As done for SIDIS, we choose  $q_T < 0.2 Q + 0.5$  GeV. Again, the values of the coefficients are chosen to maximize the goodness of the fit and to not exclude too many points. As suggested in Ref. [77], we consider the target nuclei as an ensemble composed by 40% of protons and 60% of neutrons, independent one from the other.

As we already observed, results from E288 and E605 experiments are reported as  $\frac{Ed^3\sigma}{d^3q}$ ; this variable is related to the differential cross section of Eq. (11) in the following way:

$$\frac{Ed^3\sigma}{d^3q} = \frac{d^3\sigma}{d\phi d\eta q_T dq_T} \Rightarrow \frac{d^2\sigma}{\pi d\eta d(q_T^2)} \quad (41)$$

where  $\phi$  is the polar angle of  $q_T$  and the third term is the average over  $\phi$ . Therefore, the invariant dimuon cross section can be obtained from Eq. (11) performing an integration of its terms over  $Q^2$  and adding a factor  $1/\pi$  to the result

$$\frac{Ed^3\sigma}{d^3q} = \frac{1}{\pi} \int dQ^2 \frac{d\sigma}{dQ^2 dq_T^2 d\eta}. \quad (42)$$

We checked numerically that integrating in  $Q^2$  only the prefactor  $\sigma_q^\gamma$ , defined in Eq. (12), and not the entire term in Eq. (11) (including then the convolution) introduces only a negligible error in the theoretical estimates. We also assume that  $\alpha_{\text{em}}$  does not change within the experimental bin. For Drell-Yan we thus obtain

$$\frac{1}{\pi} \int dQ^2 \frac{d\sigma}{dQ^2 dq_T^2 d\eta} \approx \frac{4\alpha_{\text{em}}^2 e_q^2 \ln\left(\frac{Q_f^2}{Q_i^2}\right)}{3N_c s} F_{UU}^1. \quad (43)$$

where  $Q_{i,f}$  are the lower and upper values in the experimental bin. As evident from Eq. (12), for  $Z$  production the integration over  $Q^2$  with the delta function yields

$$\frac{1}{\pi} \int dQ^2 \frac{d\sigma}{dQ^2 dq_T^2 d\eta} \approx \frac{\pi^2 \alpha_{\text{em}}}{s \sin^2 \theta_W \cos^2 \theta_W} B_R(Z \rightarrow \ell^+ \ell^-) F_{UU}^1 \quad (44)$$

### C. Z-boson production data

In order to reach higher  $Q$  and  $q_T$  values, we also consider  $Z$  boson production in collider experiments at Tevatron. We analyze data from CDF and D0, collected during Tevatron Run I [79, 80] at  $\sqrt{s} = 1.8$  TeV and Run II [81, 82] at  $\sqrt{s} = 1.96$  TeV. CDF and D0 collaborations studied the differential cross section for  $p\bar{p} \rightarrow Z \rightarrow e^+e^- + X$ , namely the production of an  $e^+e^-$  pair from  $p\bar{p}$  collision, through an intermediate  $Z$  vector boson.

The invariant mass distribution peaks at the  $Z$ -pole,  $Q \approx M_Z$ , while the transverse momentum of the exchanged  $Z$  ranges in  $0 < q_T < 20$  GeV. We use the same kinematic condition applied to Drell-Yan events:  $q_T < 0.2 Q + 0.5$  GeV = 18.7 GeV, since  $Q$  is fixed to  $M_Z$ .

The observable measured in CDF and D0 is  $d\sigma/dq_T$ , apart from the case of D0 Run II, for which the published data refer to  $1/\sigma \times d\sigma/dq_T$ . In order to work with the same observable in all the cases considered, we multiply the D0-Run II data by the total cross section of the process  $\sigma_{\text{exp}} = 255.8 \pm 16$  pb [83]. In this case, we add in quadrature the uncertainties of the total cross section and of the published data.

We normalize our functional form with factors listed in Tab. IV. These are the same normalization factors used in Ref. [76] to fit  $Z$  boson production and differ from the experimental ones.

### D. The replica method

Our fit is based on the replica methodology. In this section we describe this method and we give a definition of the  $\chi^2$  function minimized by the fit procedure. The fit and the error analysis are carried out using a similar Monte Carlo approach as in Refs. [23, 84, 85] and taking inspiration from the work of the Neural-Network PDF (NNPDF) collaboration (see, e.g., Refs. [86–88]). The approach consists in creating  $\mathcal{M}$  replicas of the data points. In each replica (denoted by the index  $r$ ), each data point  $i$  is shifted by a Gaussian noise with the same variance as the measurement. Each replica, therefore, represents a possible outcome of an independent experimental measurement, which we denote by  $m_{N,r}^h(x, z, \mathbf{P}_{hT}^2, Q^2)$ . The number of replicas is chosen so that the mean and standard deviation of the set of replicas accurately reproduces the original data points. In this case 200 replicas are sufficient for the purpose.

	HERMES $p \rightarrow \pi^+$	HERMES $p \rightarrow \pi^-$	HERMES $p \rightarrow K^+$	HERMES $p \rightarrow K^-$
Reference	[72]			
Cuts	$Q^2 > 1.4 \text{ GeV}^2$ $0.2 < z < 0.74$ $P_{hT} < \text{Min}[0.2 Q, 0.7 Qz] + 0.5 \text{ GeV}$			
Points	190	190	189	187
Max. $Q^2$	9.2 $\text{GeV}^2$			
$x$ range	$0.06 < x < 0.4$			

TABLE I: Semi-inclusive DIS proton-target data (Hermes experiment).

	HERMES $D \rightarrow \pi^+$	HERMES $D \rightarrow \pi^-$	HERMES $D \rightarrow K^+$	HERMES $D \rightarrow K^-$	COMPASS $D \rightarrow h^+$	COMPASS $D \rightarrow h^-$
Reference	[72]				[73]	
Cuts	$Q^2 > 1.4 \text{ GeV}^2$ $0.2 < z < 0.7$ $P_{hT} < \text{Min}[0.2 \text{ } Q, 0.7 \text{ } Qz] + 0.5 \text{ GeV}$					
Points	190	190	189	189	3125	3127
Max. $Q^2$	9.2 GeV <sup>2</sup>				10 GeV <sup>2</sup>	
$x$ range	0.06 < $x$ < 0.4				0.006 < $x$ < 0.12	
Notes					Observable: $m_{\text{norm}}(x, z, \mathbf{P}_{hT}^2, Q^2)$ , Eq. (40)	

TABLE II: Semi-inclusive DIS deuteron-target data (Hermes and Compass experiments).

	E288 200	E288 300	E288 400	E605
Reference	[77]	[77]	[77]	[78]
Cuts	$q_T < 0.2 Q + 0.5 \text{ GeV}$			
Points	45	45	78	35
$\sqrt{s}$	19.4 GeV	23.8 GeV	27.4 GeV	38.8 GeV
$Q$ range	4-9 GeV	4-9 GeV	5-9, 11-14 GeV	7-9, 10.5-18 GeV
Kin. var.	$\eta=0.4$	$\eta=0.21$	$\eta=0.03$	$x_F = 0.1$

TABLE III: Low energy Drell-Yan data collected by the E288 and E605 experiments at Tevatron, with different center-of-mass energies.

	CDF Run I	D0 Run I	CDF Run II	D0 Run II
Reference	[79]	[80]	[81]	[82]
Cuts	$q_T < 0.2 Q + 0.5 \text{ GeV} = 18.7 \text{ GeV}$			
Points	31	14	37	8
$\sqrt{s}$	1.8 TeV	1.8 TeV	1.96 TeV	1.96 TeV
Normalization	1.114	0.992	1.049	1.048

TABLE IV:  $Z$  boson production data collected by the CDF and D0 experiments at Tevatron, with different center-of-mass energies.

A minimization procedure is applied to each replica separately, by minimizing the following error function:<sup>4</sup>

$$E_r^2(\{p\}) = \sum_i \frac{\left(m_{N,r}^h(x_i, z_i, \mathbf{P}_{hTi}^2, Q_i^2) - m_{N,\text{theo}}^h(x_i, z_i, \mathbf{P}_{hTi}^2; \{p\})\right)^2}{\left(\Delta m_{N,\text{stat}}^h + \Delta m_{N,\text{sys}}^h\right)(x_i, z_i, \mathbf{P}_{hTi}^2, Q_i^2) + \left(\Delta m_{N,\text{theo}}^h(x_i, z_i, \mathbf{P}_{hTi}^2)\right)^2}. \quad (45)$$

The sum runs over the  $i$  experimental points, including all species of targets  $N$  and final-state hadrons  $h$ . In each  $z$  bin for each replica the values of the collinear fragmentation functions  $D_1^{a-h}$  are independently modified with a Gaussian noise with standard deviation equal to the theoretical error  $\Delta D_1^{a-h}$ . In this work we rely on different parametrizations for  $D_1^{a-h}$ : for pions we use the DSEHS analysis [64] at NLO in  $\alpha_S$ ; for kaons we use the DSS parametrization [65] at LO in  $\alpha_S$ . The uncertainties  $\Delta D_1^{a-h}$  are estimated from the plots in Ref. [89]; they represent the only source of uncertainty in  $\Delta m_{N,\text{theo}}^h$ . Statistical and systematic experimental uncertainties  $\Delta m_{N,\text{stat}}^h$  and  $\Delta m_{N,\text{sys}}^h$  are taken from the experimental collaborations. We do not take into account the covariance among different kinematic bins.

MINUIT minimizes the error function in Eq. (45) calculating its gradient with respect to the vector of parameters  $\{p\}$ . In each replica we randomize the starting point of the minimization, to better sample the space of fit parameters. The final outcome is a set of  $\mathcal{M}$  different vectors of best-fit parameters,  $\{p_{0r}\}$ ,  $r = 1, \dots, \mathcal{M}$ , with which we can calculate any observable, its mean, and its standard deviation. The distribution of these values needs not to be necessarily Gaussian. In fact, in this case the  $1\sigma$  confidence interval is different from the 68% interval. The latter can simply be computed for each experimental point by rejecting the largest and the lowest 16% of the  $\mathcal{M}$  values.

Although the minimization is performed on the function defined in Eq. (45), the agreement of the  $\mathcal{M}$  replicas with the original data is expressed in terms of a  $\chi^2$  function defined as in Eq. (45) but with the replacement  $m_{N,r}^h \rightarrow m_N^h$ , i.e., with respect to the original data set. If the model is able to give a good description of the data, the distribution of the  $\mathcal{M}$  values of  $\chi^2/\text{d.o.f.}$  should be peaked around one.

#### IV. RESULTS

Our work aims at simultaneously fitting for the first time data sets related to different experiments. In the past, only fits related either to SIDIS or hadronic collisions have been presented. Here we mention a selection of recent existing analyses. Among the fits of SIDIS data only, we refer to Refs. [23] and [74]. In the first one, the authors fitted HERMES multiplicities only (1538 points in total) without taking into account QCD evolution (not DGLAP, nor TMD). In this work a flavor decomposition in transverse momentum for the unpolarized TMDs and an analysis of the kinematic dependence of the intrinsic average square transverse momenta were presented. In Ref. [74] the authors fitted HERMES and COMPASS multiplicities separately (576 and 6284 points respectively), introducing an ad-hoc normalization for COMPASS data and using DGLAP evolution. A fit of SIDIS data including TMD evolution was performed on measurement by the H1 collaboration of the so-called transverse energy flow [55, 90].

Looking at data from hadronic collisions, in 2007 Konychev and Nadolsky [57] fitted data of low-energy Drell-Yan events and  $Z$ -boson production at Tevatron, taking into account TMD evolution at NLL accuracy (this is the most recent of a series of important papers on the subject [56, 75, 91]). They did not consider SIDIS events and fitted in total 98 points. Contrary to our approach, Konychev and Nadolsky studied the quality of the fit as a function of  $\xi_{\text{max}}$ . They found that the best value for  $\xi_{\text{max}}$  is  $1.5 \text{ GeV}^{-1}$ . We choose  $\xi_{\text{max}} \approx 1.123 \text{ GeV}^{-1}$ , instead (see Sec. II C). Comparisons of best-fit values in the nonperturbative Sudakov form factors are delicate, since the functional form is different from ours. In 2014 D'Alesio, Echevarria, Melis, Scimemi performed a fit [76] of Drell-Yan data and  $Z$ -boson production data at Tevatron, focusing in particular on the role of the nonperturbative contribution to the kernel of TMD evolution. This is the fit with the highest accuracy in transverse momentum resummation performed up to date (NNLL in the Sudakov exponent and  $\mathcal{O}(\alpha_S)$  in the Wilson coefficients). In the same year Echevarria, Idilbi, Kang and Vitev [15] attempted a global fit of data for the Sivers asymmetry (thus including both SIDIS and Drell-Yan events), extracting also the nonperturbative part of the unpolarized TMDs. They anyway considered only one bin in  $x, Q^2$  both for HERMES and COMPASS and the agreement between data and theory is questionable. Another attempt was performed by Sun, Isaacson, Yuan and Yuan [92] without providing a precise fit of the nonperturbative contributions.

In the following we detail the results of a fit to the data sets described in Sec. III with a a flavor-independent configuration for the transverse momentum dependence of unpolarized TMDs. In Tab. V we present the total  $\chi^2$ . The number of degrees of freedom (d.o.f.) is given by the number of data points analyzed reduced by the number of

---

<sup>4</sup> Note that the error for each replica is taken to be equal to the error on the original data points. This is consistent with the fact that the variance of the  $\mathcal{M}$  replicas should reproduce the variance of the original data points.

free parameters in the error function. The overall quality of the fit is good, with a global  $\chi^2/\text{d.o.f.} = 1.55 \pm 0.05$ . Uncertainties are computed as the 68% confidence level (C.L.) from the replica methodology.

Points	Parameters	$\chi^2$	$\chi^2/\text{d.o.f.}$
8059	11	$12629 \pm 363$	$1.55 \pm 0.05$

TABLE V: Total number of points analyzed, number of free parameters and  $\chi^2$  values.

### A. Agreement between data and theory

The partition of the global  $\chi^2$  among SIDIS off a proton, SIDIS off a deuteron, Drell-Yan and  $Z$  production events is given in Tab. VI, VII, VIII, IX respectively.

#### *Semi-inclusive DIS*

For SIDIS at HERMES off a proton, most of the contribution to the  $\chi^2$  comes from events with a  $\pi^+$  in the final state. In Ref. [23] the high  $\chi^2$  was attributed to the poor agreement between experiment and theory at the level of the collinear multiplicities. In this work we use a newer parametrization of the collinear FFs (DSEHS [64]), based on a fit which includes HERMES collinear pion multiplicities. In spite of this improvement, the contribution to  $\chi^2$  from HERMES data is higher than in Ref. [23], because the present fit includes data from other experiments (HERMES represents less than 20% of the whole data set). The bins with the worst agreement are at low  $Q^2$ . As we will discuss in Sec. IV C, we think that the main reason for the large  $\chi^2$  at HERMES is a normalization difference. This may also be due to the fact that we are computing our theoretical estimates at the average values of the kinematic variables, instead of integrating the multiplicities in each bin. Kaon multiplicities have in general a lower  $\chi^2$ , due to the bigger statistical errors and the large uncertainties for the kaon FFs.

	HERMES $p \rightarrow \pi^+$	HERMES $p \rightarrow \pi^-$	HERMES $p \rightarrow K^+$	HERMES $p \rightarrow K^-$
Points	190	190	189	187
$\chi^2/\text{points}$	$4.83 \pm 0.42$	$2.47 \pm 0.28$	$0.91 \pm 0.14$	$0.82 \pm 0.17$

TABLE VI: Number of points analyzed and  $\chi^2$  values for SIDIS off a proton target.

For pion production off a deuteron at HERMES the  $\chi^2$  is lower with respect to the production off a proton, but still compatible within uncertainties. For kaon production off a deuteron the  $\chi^2$  is higher with respect to the scattering off a proton. The difference is especially large for  $K^-$ .

SIDIS at COMPASS involves scattering off deuteron only,  $D \rightarrow h^\pm$ , and we identify  $h \equiv \pi$ . The quality of the agreement between theory and COMPASS data is better than in the case of pion production at HERMES. This depends on at least two factors: first, our fit is essentially driven by the COMPASS data, which represent about 75% of the whole data set; second, the observable that we fit in this case is the normalized multiplicity, defined in (40). This automatically eliminates most of the discrepancy between theory and data due to normalization.

	HERMES $D \rightarrow \pi^+$	HERMES $D \rightarrow \pi^-$	HERMES $D \rightarrow K^+$	HERMES $D \rightarrow K^-$	COMPASS $D \rightarrow h^+$	COMPASS $D \rightarrow h^-$
Points	190	190	189	189	3125	3127
$\chi^2/\text{points}$	$3.46 \pm 0.32$	$2.00 \pm 0.17$	$1.31 \pm 0.26$	$2.54 \pm 0.57$	$1.11 \pm 0.03$	$1.61 \pm 0.04$

TABLE VII: Number of points analyzed and  $\chi^2$  values for SIDIS off a deuteron target.

Fig. 3 presents the agreement between the theoretical formula in (3) and the HERMES multiplicities for production of pions off a proton and a deuteron. Different  $\langle x \rangle$ ,  $\langle z \rangle$  and  $\langle Q^2 \rangle$  bins are displayed as a function of the transverse

momentum of the detected hadron  $P_{hT}$ . The grey bands are an envelope of the 200 replica of best-fit curves. For every point in  $P_{hT}$  we apply a 68% C.L. selection criterion. Points marked with different symbols and colors correspond to different  $\langle z \rangle$  values. There is a strong correlation between  $\langle x \rangle$  and  $\langle Q^2 \rangle$  that does not allow to explore  $x$  and  $Q^2$  dependence of the TMDs separately. Studying the contributions to the  $\chi^2/\text{points}$  as a function of the kinematics, we notice that the  $\chi^2(Q^2)$  tends to improve as we move to higher  $Q^2$  values, where the kinematic approximations of factorization are more reliable. Moreover, usually the  $\chi^2(z)$  increases at lower  $z$  values.

Fig. 4 has same contents and notation as in Fig. 3 but for kaons in the final state. In this case, the trend of the agreement as a function of  $Q^2$  is not as clear as for the case of pions: good agreement is found also at low  $Q^2$ .

In Fig. 5 we present COMPASS normalized multiplicities (see Eq. (40)) for production of  $\pi^-$  off a deuteron for different  $\langle x \rangle$ ,  $\langle z \rangle$ , and  $\langle Q^2 \rangle$  bins as a function of the transverse momentum of the detected hadron  $P_{hT}$ . The open marker around the first  $P_{hT}$  point in each panel indicates that the first value is fixed and not fitted. The correlation between  $x$  and  $Q^2$  is less strong than at HERMES and this allows us to study different  $\langle x \rangle$  bins at fixed  $\langle Q^2 \rangle$ . For the highest  $Q^2$  bins, the agreement is good for all  $\langle x \rangle$ ,  $\langle z \rangle$  and  $P_{hT}^2$ . In bins at lower  $Q^2$ , the descriptions gets worse, especially at low and high  $z$ . For fixed  $\langle Q^2 \rangle$  and high  $\langle z \rangle$ , a good agreement is recovered moving to higher  $\langle x \rangle$  bins (see, e.g., the third line from the top in Fig. 5).

Fig. 6 has same content and notation as in Fig. 5, but for  $h^+ \equiv \pi^+$ . The same comments on the agreement between theory and the data apply.

### *Drell-Yan and Z production*

The low energy Drell-Yan data collected by the E288 and E605 experiments at Fermilab have large error bands (see Fig. 7). This is why the  $\chi^2$  values in Tab. VIII are rather low compared to the other data sets.

The agreement is also good for  $Z$  boson production, see Tab. IX. The statistics from Run-II is higher, which generates smaller experimental uncertainties and higher  $\chi^2$ , especially for the CDF experiment.

	E288 [200]	E288 [300]	E288 [400]	E605
Points	45	45	78	35
$\chi^2/\text{points}$	$0.99 \pm 0.09$	$0.84 \pm 0.10$	$0.32 \pm 0.01$	$1.12 \pm 0.08$

TABLE VIII: Number of points analyzed and  $\chi^2$  values for fixed-target Drell-Yan experiments at low energy. The labels in square brackets were introduced in Sec. III B.

	CDF Run I	D0 Run I	CDF Run II	D0 Run II
Points	31	14	37	8
$\chi^2/\text{points}$	$1.36 \pm 0.00$	$1.11 \pm 0.02$	$2.00 \pm 0.02$	$1.73 \pm 0.01$

TABLE IX: Number of points analyzed and  $\chi^2$  values for  $Z$  boson production at Tevatron.

Fig. 7 displays the cross section for DY events differential with respect to the transverse momentum  $q_T$  of the virtual photon, its invariant mass  $Q^2$  and rapidity  $y$ . As for the case of SIDIS, the grey bands are the 68% C.L. envelope of the 200 replicas of the fit function. The four panels represents different values for the rapidity  $y$  or  $x_F$  (see Eq. (14)). In each panel, we have plots for different  $Q^2$  values. The lower is  $Q$ , the less points in  $q_T$  we fit (see also Sec. III B). The hard scale lies in the region  $4.5 < \langle Q \rangle < 13.5$  GeV. This region is of particular importance, since these “moderate”  $Q$  values should be high enough to safely apply factorization and, at the same time, low enough in order for the nonperturbative effects to not be shaded by transverse momentum resummation.

In Fig. 8 we compare the cross section differential with respect to the transverse momentum  $q_T$  of the virtual  $Z$  (namely Eq. (11) integrated over  $\eta$ ) with data from CDF and D0 at Tevatron Run I and II. Due to the higher  $Q = M_Z$ , the range explored in  $q_T$  is much larger compared to all the other observables considered. The tails of the distributions deviate from a Gaussian behavior, as it is also evident in the bins at higher  $Q^2$  in Fig. 7. The band from the replica methodology in this case is much narrower, due to the reduced sensitivity to the intrinsic transverse momenta at  $Q = M_Z$  and to the limited range of best-fit values for the parameter  $g_2$ , which controls soft-gluon emission. As an effect of TMD evolution, the peak shifts from  $\sim 1$  GeV for Drell-Yan events in Fig. 7 to  $\sim 5$  GeV in Fig. 8. The position of the peak is affected both by the perturbative and the nonperturbative part of the Sudakov exponent (see

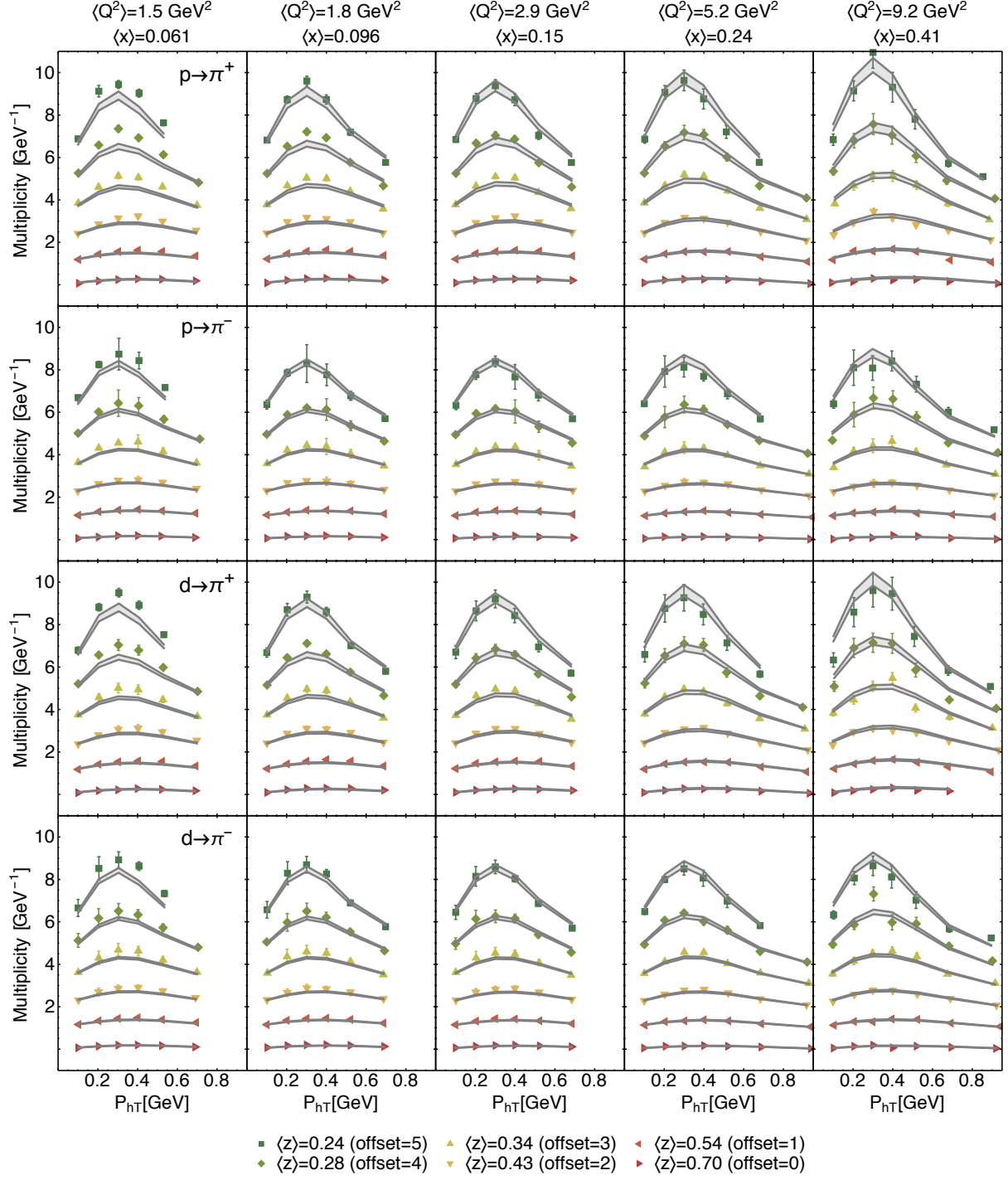


FIG. 3: Hermes multiplicities for production of pions off a proton and a deuteron for different  $\langle x \rangle$ ,  $\langle z \rangle$ , and  $\langle Q^2 \rangle$  bins as a function of the transverse momentum of the detected hadron  $P_{hT}$ . For clarity, each  $\langle z \rangle$  bin has been shifted by an offset indicated in the legend.

Sec. II C and [22]). Most of the contributions to the  $\chi^2$  comes from normalization effects and not from the shape in  $q_T$  (see Sec. IV C).

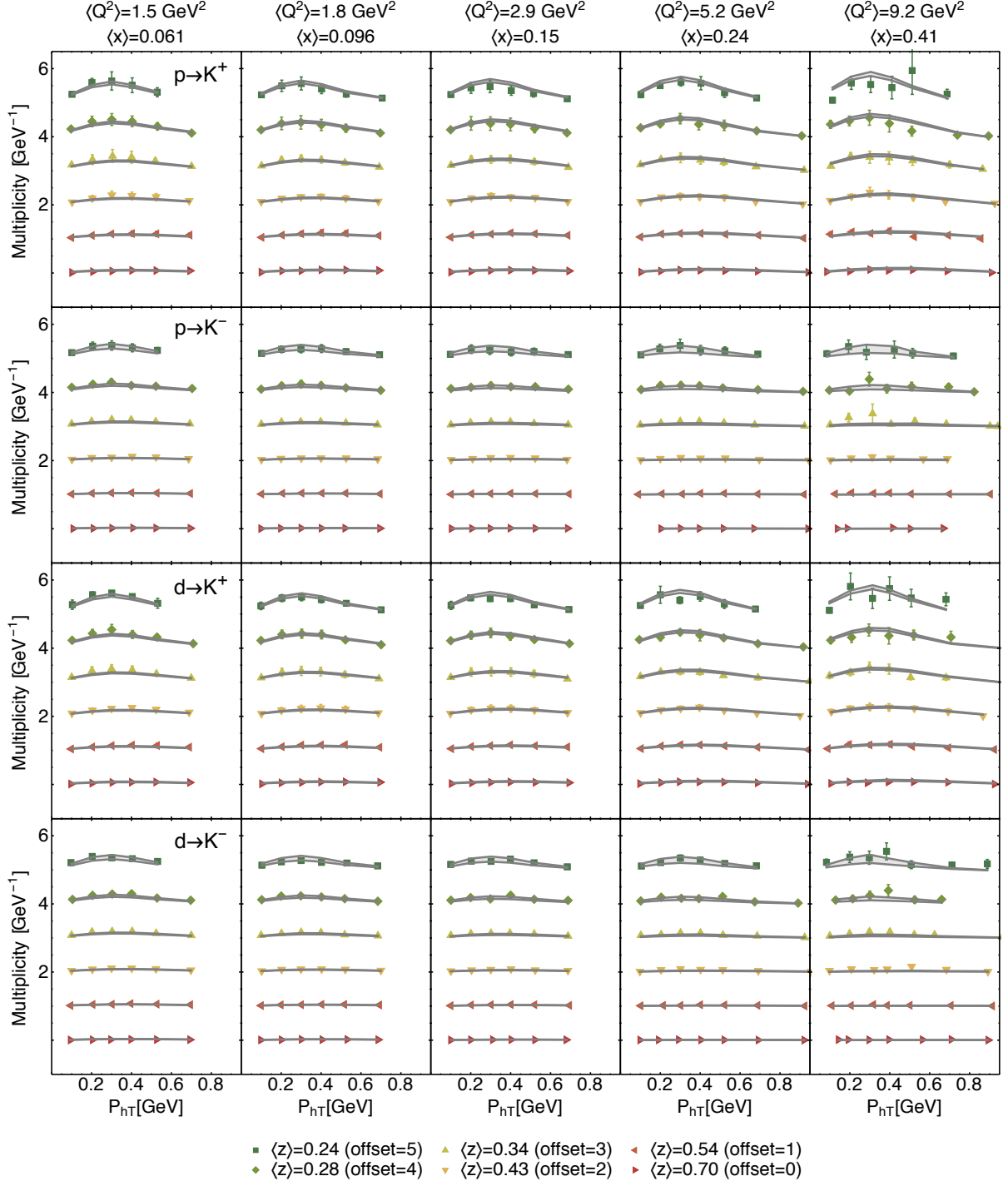


FIG. 4: Hermes multiplicities for production of kaons off a proton and a deuteron for different  $\langle x \rangle$ ,  $\langle z \rangle$ , and  $\langle Q^2 \rangle$  bins as a function of the transverse momentum of the detected hadron  $P_{hT}$ . For clarity, each  $\langle z \rangle$  bin has been shifted by an offset indicated in the legend.



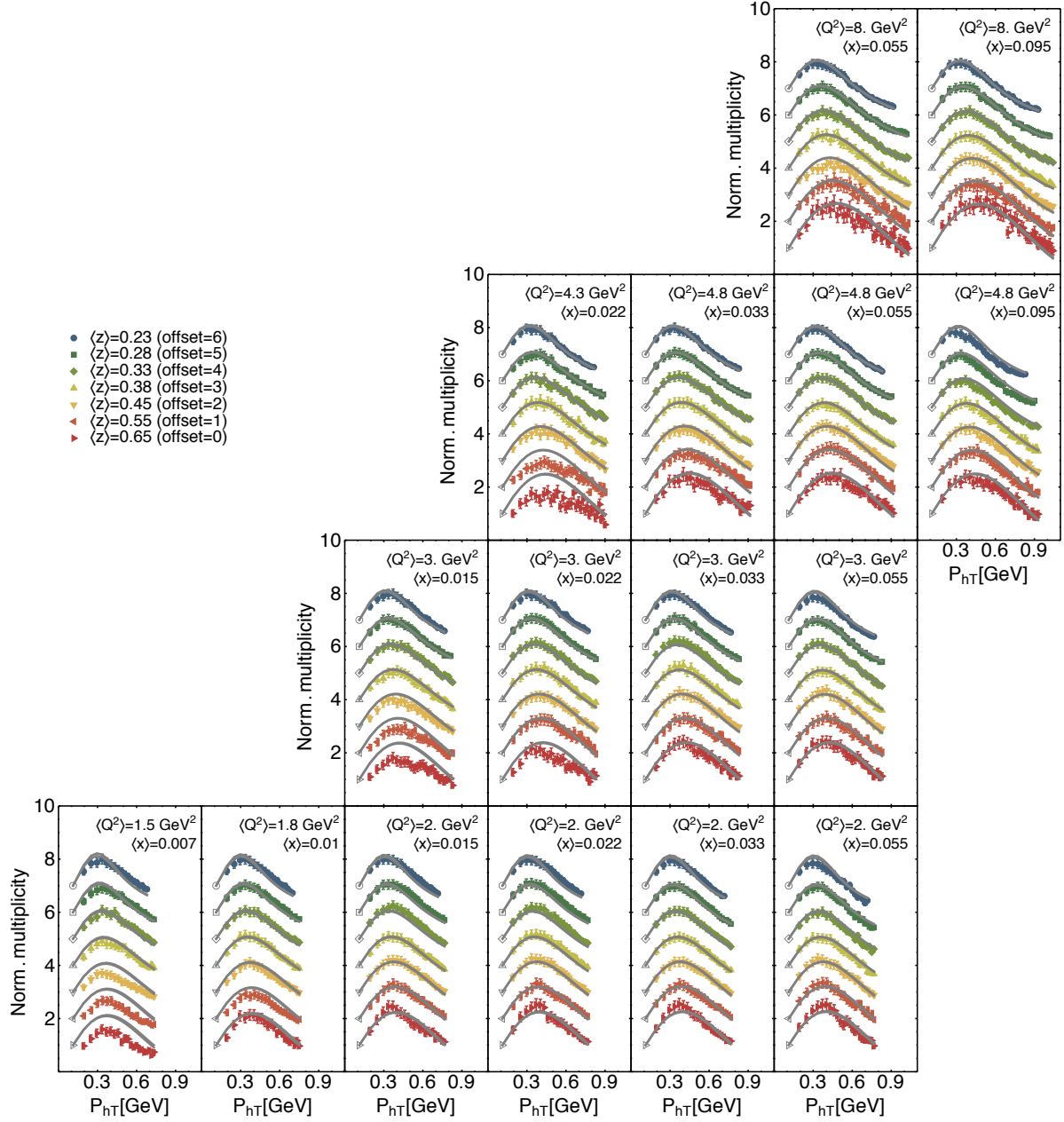


FIG. 5: Compass multiplicities for production of negative hadrons ( $\pi^-$ ) off a deuteron for different  $\langle x \rangle$ ,  $\langle z \rangle$ , and  $\langle Q^2 \rangle$  bins as a function of the transverse momentum of the detected hadron  $P_{hT}$ . Multiplicities are normalized to the first bin in  $P_{hT}$  for each  $\langle z \rangle$  value (see (40)). For clarity, each  $\langle z \rangle$  bin has been shifted by an offset indicated in the legend.

### B. Transverse momentum dependence at 1 GeV

The variables  $\xi_{\min}$  and  $\xi_{\max}$  delimit the range in  $\xi_T$  where transverse momentum resummation is computed perturbatively.  $\xi_{\max}$  allows to avoid the Landau pole and  $\xi_{\min}$  allows to recover correctly the high transverse momentum limit of the cross section (see also Sec. IIC). The  $g_2$  parameter enters the nonperturbative Sudakov exponent and

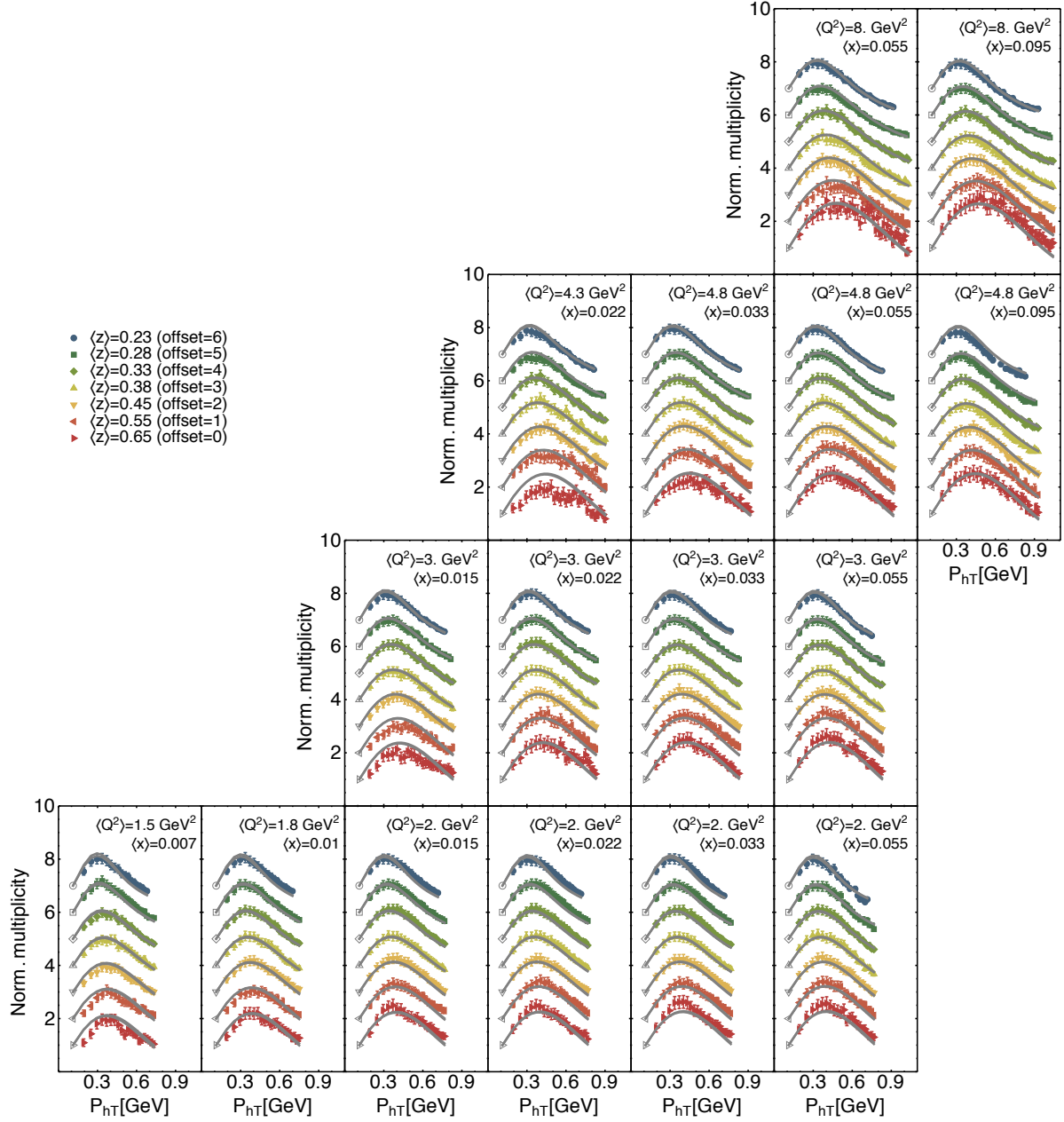


FIG. 6: Compass multiplicities for production of positive hadrons ( $\pi^+$ ) off a deuteron for different  $\langle x \rangle$ ,  $\langle z \rangle$ , and  $\langle Q^2 \rangle$  bins as a function of the transverse momentum of the detected hadron  $P_{hT}$ . Multiplicities are normalized to the first bin in  $P_{hT}$  for each  $\langle z \rangle$  value (see (40)). For clarity, each  $\langle z \rangle$  bin has been shifted by an offset indicated in the legend.

quantifies the amount of transverse momentum due to soft gluon radiation that is not included in the perturbative part of the Sudakov form factor. As already detailed in Sec. II C, in this work we fix the value for  $\xi_{\min}$  and  $\xi_{\max}$  in such a way that at  $Q = 1$  GeV the unpolarized TMDs coincide with their nonperturbative input.  $g_2$ , instead, is a fit parameter.

Tab. X summarizes the chosen values of  $\xi_{\min}$ ,  $\xi_{\max}$  and the best-fit value for  $g_2$ . The latter is given as an average

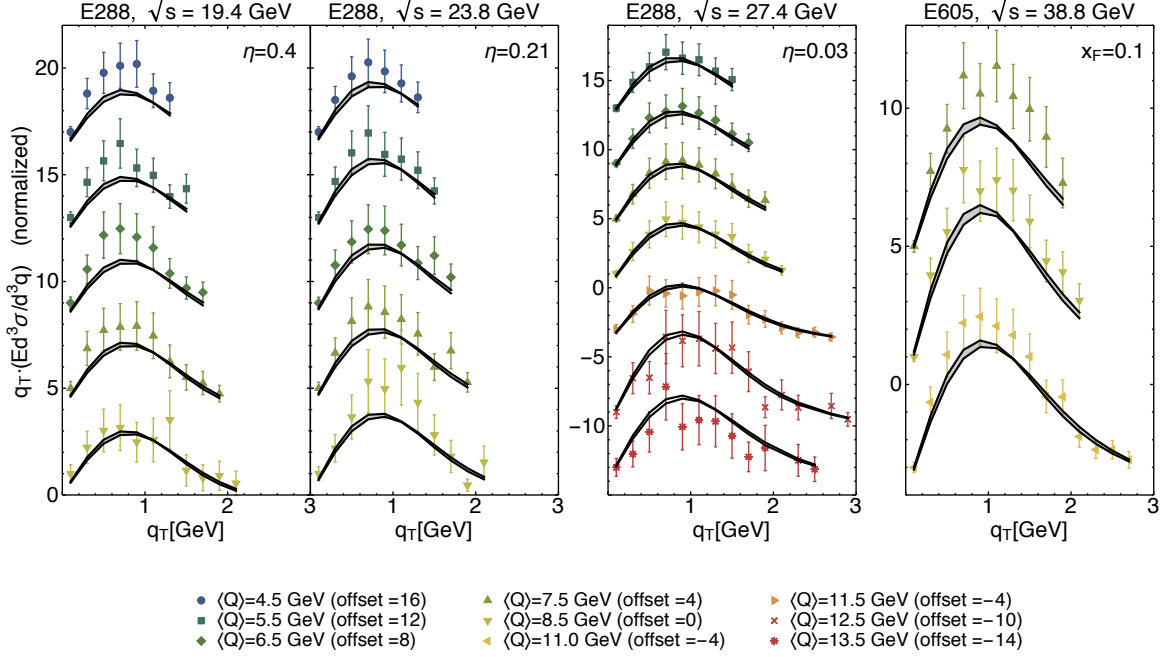


FIG. 7: Drell-Yan differential cross section for different experiments and different values of  $\sqrt{s}$  and for different  $\langle Q \rangle$  bins. For clarity, each  $\langle Q \rangle$  bin has been normalized (the first data point has been set always equal to 1) and then shifted by an offset indicated in the legend.

with 68% C.L. uncertainty computed over the set of 200 replicas. A larger value ( $g_2 = 0.184 \pm 0.018$ ) was found in Ref. [57], where however no SIDIS data was taken into consideration. We stress here that a prescription involving both  $\xi_{\min}$  and  $\xi_{\max}$  is equivalent to requesting  $\mu_b^2 < Q^2$  for all  $\xi_T$  values in Eq. (29). This requirement turns out to be useful in order to fit SIDIS data with TMD evolution.

To make it possible to analyze the results related to a single replica, instead of the full set, we also quote the results obtained from replica 105, since its parameters are very close to the mean values of all replicas.

Tab. XI collects the best-fit values of parameters in the nonperturbative part of the TMDs at  $Q = 1$  GeV (see Eq. (33) and (34)); as for  $g_2$ , we give the average value over the full set of replicas and the standard deviation based on a 68% C.L. (see Sec. IIID), and also quote the value of replica 105.

Keeping in mind that  $\langle \hat{k}_\perp^2 \rangle = \langle \mathbf{k}_\perp^2 \rangle(x = 0.1)$  and  $\langle \hat{P}_\perp^2 \rangle = \langle \mathbf{P}_\perp^2 \rangle(z = 0.5)$ , we note that delicate, since here we rely on a modified Gaussian ansatz, see (35) and (36). **Do we agree on the fact that  $\langle P_\perp^2 \rangle$  does not make sense here? We should remove it.**

Fig. 9 is useful to compare different extractions of partonic transverse momenta. The horizontal axis shows the value of  $\langle \hat{k}_\perp^2(x) \rangle$  (average transverse momentum squared of the TMD PDFs) at the reference point  $x = 0.1$ . The vertical axis shows the value of  $\langle \hat{P}_\perp^2 \rangle$  (average transverse momentum squared of the TMD FFs) at  $z = 0.5$ . The white square (label 1) indicates the average values of the two quantities obtained in the present analysis at  $Q^2 = 1$  GeV<sup>2</sup>. Each black dot around the white square is an outcome of one replica. The red region around the white square contains the 68% of the replicas that are closest to the average value. The same applies to the white circle and the orange region around it (label 2), related to the flavor-independent version of the analysis in Ref. [23], obtained by fitting only HERMES SIDIS data at an average  $\langle Q^2 \rangle = 2.4$  GeV<sup>2</sup>, neglecting TMD evolution. A strong anticorrelation between the transverse momenta is evident in this older analysis. In our new analysis, the inclusion of Drell-Yan and  $Z$  production data adds physical information about TMD PDFs, free from the influence of TMD FFs. This reduces significantly correlation between  $\langle \hat{k}_\perp^2 \rangle$  and  $\langle \hat{P}_\perp^2 \rangle$ . The 68% confidence region is smaller than in the older analysis. The average values of  $\langle \hat{k}_\perp^2 \rangle$  are similar and compatible within error bands. The values of  $\langle \hat{P}_\perp^2 \rangle$  in the present analysis turn out to be larger than in the older analysis, an effect that is due mainly to COMPASS data. It must be kept in mind that the two analyses lead also to differences in the  $x$  and  $z$  dependence of the transverse momentum squared. The kinematic dependence is shown in Fig. 10 (a) for  $\langle \mathbf{k}_\perp^2 \rangle(x)$  and Fig. 10 (b) for  $\langle \mathbf{P}_\perp^2 \rangle(z)$ . The bands are computed

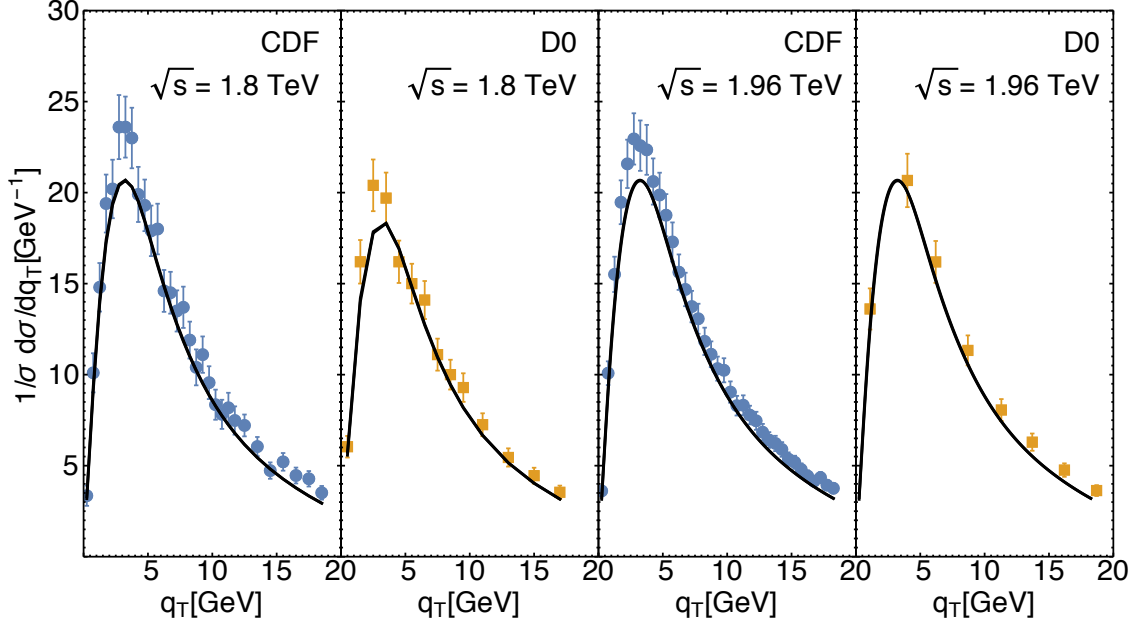


FIG. 8: Cross section differential with respect to the transverse momentum  $q_T$  of a  $Z$  boson produced from  $p\bar{p}$  collisions at Tevatron. The four panels refer to different experiments (CDF and D0) with two different values for the center-of-mass energy ( $\sqrt{s} = 1.8$  TeV and  $\sqrt{s} = 1.96$  TeV). In this case the band is narrow due to the narrow range for the best-fit values of  $g_2$ .

as the 68% C.L. envelope of the full sets of curves from the 200 replicas. Comparison with other extractions are presented and the legend is detailed in the caption of Fig. 9.

	$\xi_{\max}$ [GeV $^{-1}$ ] (fixed)	$\xi_{\min}$ [GeV $^{-1}$ ] (fixed)	$g_2$ [GeV $^2$ ]
All replicas	$2e^{-\gamma_E}$	$2e^{-\gamma_E}/Q$	$0.13 \pm 0.01$
Replica 105	$2e^{-\gamma_E}$	$2e^{-\gamma_E}/Q$	0.128

TABLE X: Values of parameters common to TMD PDFs and TMD FFs.

TMD PDFs	$g_1$ [GeV $^2$ ]	$\alpha$	$\sigma$		$\lambda$ [GeV $^{-2}$ ]	
All replicas	$0.28 \pm 0.06$	$2.95 \pm 0.05$	$0.17 \pm 0.02$		$0.86 \pm 0.78$	
Replica 105	0.285	2.98	0.173		0.39	
TMD FFs	$g_3$ [GeV $^2$ ]	$\beta$	$\delta$	$\gamma$	$\lambda_F$ [GeV $^{-2}$ ]	$g_4$ [GeV $^2$ ]
All replicas	$0.21 \pm 0.02$	$1.65 \pm 0.49$	$2.28 \pm 0.46$	$0.14 \pm 0.07$	$5.50 \pm 1.23$	$0.13 \pm 0.01$
Replica 105	0.212	2.10	2.52	0.094	5.29	0.135

TABLE XI: 68% confidence intervals of best-fit values for parametrizations of TMDs at  $Q = 1$  GeV.

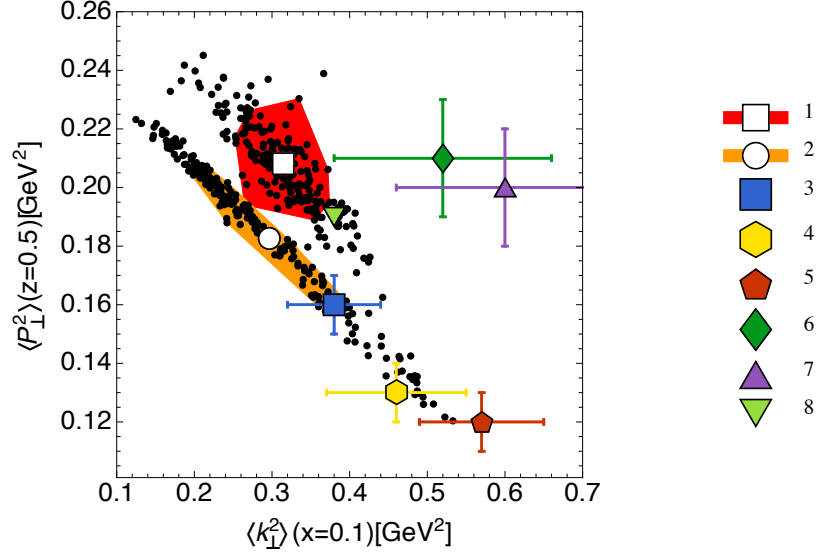


FIG. 9: Correlation between transverse momenta in TMD FFs,  $\langle P_{\perp}^2 \rangle(z = 0.5)$ , and in TMD PDFs,  $\langle k_{\perp}^2 \rangle(x = 0.1)$ , in different phenomenological extractions. (1): average values (white square) obtained in the present analysis, values obtained from each replica (black dots) and 68% C.L. area (red); (2) results from Ref. [23], (3) results from Ref. [93], (4) results from Ref. [74] for HERMES data, (5) results from Ref. [74] for HERMES data at high  $z$ , (6) results from Ref. [74] for normalized COMPASS data, (7) results from Ref. [74] for normalized COMPASS data at high  $z$ , (8) results from Ref. [15].

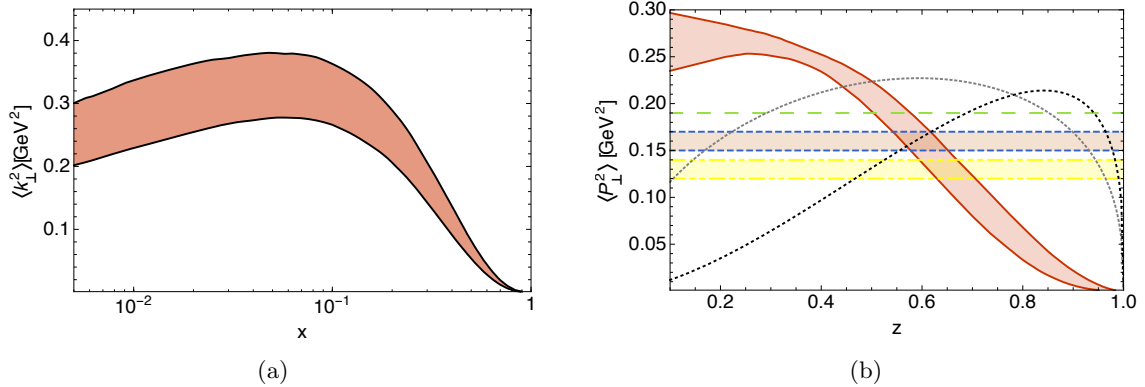


FIG. 10: Kinematic dependence of  $\langle k_{\perp}^2 \rangle(x)$  (a) and of  $\langle P_{\perp}^2 \rangle(z)$  (b). The bands are the 68% C.L. envelope of the full sets of best-fit curves. **We should put the figures without comparisons to other cases.**

### C. Modifications to the default choices

In this subsection we discuss the effect of modifying some of the choices we made in our default fit. Instead of repeating the fitting procedure with different choices, we limited ourselves to checking how the  $\chi^2$  of a single replica is affected by the modifications.

As starting point we chose replica 105, which, as discussed above, is one of the most representative among the whole replica set. The global  $\chi^2/\text{d.o.f.}$  of replica 105 is 1.51. We kept all parameters fixed, without performing any new minimization, and we computed the  $\chi^2$  after the modifications described in the following.

First of all, we analyzed HERMES data with the same strategy as COMPASS, i.e., we normalized HERMES data to the value of the first bin in  $P_{hT}$ . In this case, the global  $\chi^2/\text{d.o.f.}$  reduces sharply to 1.27. The partial  $\chi^2$  for the different SIDIS processes measured at HERMES are shown in Table XII. This confirms that normalization effects are the main contribution to the  $\chi^2$  of SIDIS data and have minor effects on TMD-related parameters. In fact, even if we

perform a new fit with this modification, the  $\chi^2$  does not improve significantly and parameters do not change much.

	$p \rightarrow \pi^+$	$p \rightarrow \pi^-$	$p \rightarrow K^+$	$p \rightarrow K^-$	$D \rightarrow \pi^+$	$D \rightarrow \pi^-$	$D \rightarrow K^+$	$D \rightarrow K^-$
Original	5.18	2.67	0.75	0.78	3.63	2.31	1.12	2.27
Normalized	1.94	1.13	0.57	0.29	1.59	0.80	0.47	0.97

TABLE XII:  $\chi^2/\text{d.o.f.}$  for HERMES data with and without normalization to the value of the first bin in  $P_{hT}$ .

We also considered the effect of changing the normalization of the  $Z$ -boson data: if we increase the normalization factors quoted in the last row of Tab. IV by 5%, the  $\chi^2$  quoted in the last row of Tab. IX drop to 0.66, 0.52, 0.65, 0.68. This effect is also already visible by eye in Fig. 8: the theoretical curves are systematically below the experimental data points, but the shape is reproduced very well.

We considered the sensitivity of our results to the set of parameterizations adopted for the collinear quark PDFs. The  $\chi^2/\text{d.o.f.}$  varies from its original value 1.51, obtained with the NLO GJR 2008 parametrization [62], to 1.84 using NLO MSTW 2008 [94], and 1.85 using NLO CJ12 [95]. In both cases, the agreement with HERMES and  $Z$  boson data is not affected significantly, the agreement with COMPASS data becomes slightly worse, and the agreement with DY data is clearly worse.

An extremely important point is the choice of kinematic cuts. Our default choices are listed in Tabs. I–IV. We considered more stringent kinematic cuts on SIDIS data:  $Q^2 > 1.5 \text{ GeV}^2$  and  $z$  range to  $0.25 < z < 0.6$  instead of  $Q^2 > 1.4 \text{ GeV}^2$  and  $0.2 < z < 0.7$ , leaving the other ones unchanged. The number of bins with these cuts reduces from 8059 to 5679 and the  $\chi^2/\text{d.o.f.}$  decreases to the value 1.23. In addition, if we replace the constraint  $P_{hT} < \text{Min}[0.2Q, 0.7Qz] + 0.5 \text{ GeV}$  with  $P_{hT} < \text{Min}[0.2Q, 0.5Qz] + 0.3 \text{ GeV}$ , the number of bins reduces to 3380 and the  $\chi^2/\text{d.o.f.}$  decreases further to 0.96. By adopting the even stricter cut  $P_{hT} < 0.2Qz$ , the number of bins drops to only 477, with a  $\chi^2/\text{d.o.f.} = 1.02$ . We can conclude that our fit, obtained by fitting data in an extended kinematic region, where TMD factorization may be questioned, works extremely well also in a narrower region, where TMD factorization is expected to be under control.

## V. CONCLUSIONS

In this work we demonstrated for the first time that it is possible to perform a simultaneous fit of unpolarized TMDs PDFs and FFs to data of SIDIS, Drell-Yan, and  $Z$  boson production collected by different experiments. This constitutes the first attempt towards a global fit of  $f_1^a(x, k_\perp^2)$  and  $D_1^{a \rightarrow h}(z, P_\perp^2)$  in the context of TMD factorization and with the implementation of TMD evolution at NLL accuracy and at LO in  $\alpha_S$ .

We extracted unpolarized TMDs using 8059 data points with 11 free parameters using a replica methodology. We selected data with  $Q^2 > 1.4 \text{ GeV}^2$  and  $0.2 < z < 0.7$ . We restricted our fit to the small transverse momentum region, selecting the maximum value of transverse momentum on the basis of phenomenological considerations (see Sec. III). With these choices, we included regions where TMD factorization could be questioned, but we checked that our results describe very well the regions where TMD factorization certainly holds. The average  $\chi^2/\text{d.o.f.}$  is  $1.55 \pm 0.05$ . Most of the discrepancies between experimental data and theory comes from the normalization and not from the transverse momentum shape.

Our fit is performed assuming that the intrinsic transverse momentum dependence of TMD PDFs and FFs can be parametrized by a normalized linear combination of a Gaussian and a weighted Gaussian. For the nonperturbative component of TMD evolution, we adopted the choice most often used in the literature.

We plan to release grids of the parametrizations studied in this work via TMDlib [96] to facilitate phenomenological studies for present and future experiments.

In future studies, different functional forms for all nonperturbative ingredients should be explored, adding also a possible flavor dependence, which we presently neglected. A more precise analysis from the perturbative point of view is also needed, which should in principle make it possible to describe data at higher transverse momenta and should be properly matched to the collinear fixed-order calculations.

Together with an improved theoretical framework, in order to better understand the formalism more experimental data is needed. It would be particularly useful to extend the coverage in  $x$ ,  $z$ , rapidity, and  $Q^2$ . The 12 GeV physics program at Jefferson Lab [97] will be very important to constrain TMD distributions at large  $x$ . Additional data from SIDIS (at COMPASS, at a future Electron-Ion Collider), Drell-Yan (at COMPASS, at Fermilab),  $Z/W$  production (at LHC, RHIC, and at A Fixed-Target Experiment at the LHC [98]) will be very important. Measurements related

to unpolarized TMD FFs at  $e^+e^-$  colliders (at Belle-II, BES-III, at a future International Linear Collider) will be invaluable, since they are presently missing.

Our work focused on quark TMDs. We remark that at present almost nothing is known experimentally about gluon TMDs [11, 99], because they typically require higher-energy scattering processes and they are harder to isolate as compared to quark distributions. Several promising measurements have been proposed in order to extract both the unpolarized and linearly polarized gluon TMDs inside an unpolarized proton. The cleanest possibility would be to look at dijet and heavy quark pair production in electron-proton collisions at a future EIC [100, 101]. Other proposals include isolated photon-pair production at RHIC [102] and quarkonium production at the LHC [103–105].

Testing the formalism of TMD factorization and understanding the structure of unpolarized TMDs is only the first crucial step in the exploration of the 3D proton structure in momentum space and this work opens the way to global determinations of TMDs. Building on this, we can proceed to deepen our understanding of hadron structure via polarized structure function and asymmetries (see, e.g., Refs [106–108]) and, at the same time, to test the impact of hadron structure in precision measurements at high-energies, such as at the LHC. A detailed mapping of hadron structure is essential to interpret data from hadronic collisions, which are among the most powerful tools to look for footprints of new physics.

### Acknowledgments

Discussions with Giuseppe Bozzi are gratefully acknowledged. This work is supported by the European Research Council (ERC) under the European Union’s Horizon 2020 research and innovation program (grant agreement No. 647981, 3DSPIN). AS acknowledges support from U.S. Department of Energy contract DE-AC05-06OR23177, under which Jefferson Science Associates, LLC, manages and operates Jefferson Lab. The work of AS has been funded partly also by the program of the Stichting voor Fundamenteel Onderzoek der Materie (FOM), which is financially supported by the Nederlandse Organisatie voor Wetenschappelijk Onderzoek (NWO).

- 
- [1] J. C. Collins, D. E. Soper, and G. F. Sterman, *Adv. Ser. Direct. High Energy Phys.* **5**, 1 (1989), hep-ph/0409313.
  - [2] J. Collins, *Foundations of perturbative QCD* (Cambridge University Press, 2013), ISBN 9781107645257, 9781107645257, 9780521855334, 9781139097826, URL <http://www.cambridge.org/de/knowledge/isbn/item5756723>.
  - [3] R. Angeles-Martinez et al., *Acta Phys. Polon.* **B46**, 2501 (2015), 1507.05267.
  - [4] T. C. Rogers, *Eur. Phys. J.* **A52**, 153 (2016), 1509.04766.
  - [5] A. Bacchetta, *Eur. Phys. J.* **A52**, 163 (2016).
  - [6] M. Radici, *AIP Conf. Proc.* **1735**, 020003 (2016).
  - [7] P. J. Mulders and R. D. Tangerman, *Nucl. Phys.* **B461**, 197 (1996), [Erratum: *Nucl. Phys.*B484,538(1997)], hep-ph/9510301.
  - [8] A. Bacchetta, M. Diehl, K. Goeke, A. Metz, P. J. Mulders, and M. Schlegel, *JHEP* **02**, 093 (2007), hep-ph/0611265.
  - [9] D. Boer and P. J. Mulders, *Phys. Rev.* **D57**, 5780 (1998), hep-ph/9711485.
  - [10] A. Bacchetta and P. J. Mulders, *Phys. Rev.* **D62**, 114004 (2000), hep-ph/0007120.
  - [11] P. J. Mulders and J. Rodrigues, *Phys. Rev.* **D63**, 094021 (2001), hep-ph/0009343.
  - [12] D. Boer, S. Cotogno, T. van Daal, P. J. Mulders, A. Signori, and Y.-J. Zhou, *JHEP* **10**, 013 (2016), 1607.01654.
  - [13] A. Bacchetta and M. Radici, *Phys. Rev. Lett.* **107**, 212001 (2011), 1107.5755.
  - [14] M. Anselmino, M. Boglione, and S. Melis, *Phys. Rev.* **D86**, 014028 (2012), 1204.1239.
  - [15] M. G. Echevarria, A. Idilbi, Z.-B. Kang, and I. Vitev, *Phys. Rev.* **D89**, 074013 (2014), 1401.5078.
  - [16] M. Anselmino, M. Boglione, U. D’Alesio, F. Murgia, and A. Prokudin (2016), 1612.06413.
  - [17] Z. Lu and I. Schmidt, *Phys. Rev.* **D81**, 034023 (2010), 0912.2031.
  - [18] V. Barone, M. Boglione, J. O. Gonzalez Hernandez, and S. Melis, *Phys. Rev.* **D91**, 074019 (2015), 1502.04214.
  - [19] C. Lefky and A. Prokudin, *Phys. Rev.* **D91**, 034010 (2015), 1411.0580.
  - [20] M. Anselmino, M. Boglione, U. D’Alesio, S. Melis, F. Murgia, and A. Prokudin, *Phys. Rev.* **D87**, 094019 (2013), 1303.3822.
  - [21] Z.-B. Kang, A. Prokudin, P. Sun, and F. Yuan, *Phys. Rev.* **D93**, 014009 (2016), 1505.05589.
  - [22] A. Signori, Ph.D. thesis, Vrije U., Amsterdam (2016), URL <http://inspirehep.net/record/1493030/files/Thesis-2016-Signori.pdf>.
  - [23] A. Signori, A. Bacchetta, M. Radici, and G. Schnell, *JHEP* **11**, 194 (2013), 1309.3507.
  - [24] A. Bacchetta, M. G. Echevarria, P. J. G. Mulders, M. Radici, and A. Signori, *JHEP* **11**, 076 (2015), 1508.00402.
  - [25] J. Collins, L. Gamberg, A. Prokudin, T. C. Rogers, N. Sato, and B. Wang, *Phys. Rev.* **D94**, 034014 (2016), 1605.00671.
  - [26] D. Boer et al. (2011), 1108.1713.
  - [27] A. Bacchetta, D. Boer, M. Diehl, and P. J. Mulders, *JHEP* **08**, 023 (2008), 0803.0227.
  - [28] S. Chekanov et al. (ZEUS), *Phys. Lett.* **B682**, 8 (2009), 0904.1092.
  - [29] V. Andreev et al. (H1), *Eur. Phys. J.* **C74**, 2814 (2014), 1312.4821.

- [30] J. C. Collins and D. E. Soper, Nucl. Phys. **B193**, 381 (1981), [Erratum: Nucl. Phys.B213,545(1983)].
- [31] J. C. Collins, D. E. Soper, and G. F. Sterman, Nucl. Phys. **B250**, 199 (1985).
- [32] X.-d. Ji and F. Yuan, Phys. Lett. **B543**, 66 (2002), hep-ph/0206057.
- [33] X.-d. Ji, J.-p. Ma, and F. Yuan, Phys. Rev. **D71**, 034005 (2005), hep-ph/0404183.
- [34] S. M. Aybat and T. C. Rogers, Phys. Rev. **D83**, 114042 (2011), 1101.5057.
- [35] M. G. Echevarria, A. Idilbi, and I. Scimemi, JHEP **07**, 002 (2012), 1111.4996.
- [36] M. G. Echevarria, A. Idilbi, A. Schäfer, and I. Scimemi, Eur. Phys. J. **C73**, 2636 (2013), 1208.1281.
- [37] J. C. Collins and T. C. Rogers, Phys. Rev. **D87**, 034018 (2013), 1210.2100.
- [38] H. H. Matevosyan, W. Bentz, I. C. Cloet, and A. W. Thomas, Phys. Rev. **D85**, 014021 (2012), 1111.1740.
- [39] M. Boglione, J. Collins, L. Gamberg, J. O. Gonzalez-Hernandez, T. C. Rogers, and N. Sato, Phys. Lett. **B766**, 245 (2017), 1611.10329.
- [40] E. Moffat, W. Melnitchouk, T. C. Rogers, and N. Sato (2017), 1702.03955.
- [41] M. G. Echevarria, I. Scimemi, and A. Vladimirov, JHEP **09**, 004 (2016), 1604.07869.
- [42] D. Boer and W. Vogelsang, Phys. Rev. **D74**, 014004 (2006), hep-ph/0604177.
- [43] S. Arnold, A. Metz, and M. Schlegel, Phys. Rev. **D79**, 034005 (2009), 0809.2262.
- [44] C. Patrignani et al. (Particle Data Group), Chin. Phys. **C40**, 100001 (2016).
- [45] M. Lambertsen and W. Vogelsang, Phys. Rev. **D93**, 114013 (2016), 1605.02625.
- [46] G. Parisi and R. Petronzio, Nucl. Phys. **B154**, 427 (1979).
- [47] G. Altarelli, R. K. Ellis, M. Greco, and G. Martinelli, Nucl. Phys. **B246**, 12 (1984).
- [48] G. Bozzi, S. Catani, G. Ferrera, D. de Florian, and M. Grazzini, Phys. Lett. **B696**, 207 (2011), 1007.2351.
- [49] D. Boer and W. J. den Dunnen, Nucl. Phys. **B886**, 421 (2014), 1404.6753.
- [50] E. Laenen, G. F. Sterman, and W. Vogelsang, Phys. Rev. Lett. **84**, 4296 (2000), hep-ph/0002078.
- [51] J.-w. Qiu and X.-f. Zhang, Phys. Rev. **D63**, 114011 (2001), hep-ph/0012348.
- [52] C. T. H. Davies and W. J. Stirling, Nucl. Phys. **B244**, 337 (1984).
- [53] S. Frixione, P. Nason, and G. Ridolfi, Nucl. Phys. **B542**, 311 (1999), hep-ph/9809367.
- [54] G. Bozzi, S. Catani, D. de Florian, and M. Grazzini, Nucl. Phys. **B737**, 73 (2006), hep-ph/0508068.
- [55] P. M. Nadolsky, D. R. Stump, and C. P. Yuan, Phys. Rev. **D61**, 014003 (2000), [Erratum: Phys. Rev.D64,059903(2001)], hep-ph/9906280.
- [56] F. Landry, R. Brock, P. M. Nadolsky, and C. P. Yuan, Phys. Rev. **D67**, 073016 (2003), hep-ph/0212159.
- [57] A. V. Konychev and P. M. Nadolsky, Phys. Lett. **B633**, 710 (2006), hep-ph/0506225.
- [58] C. A. Aidala, B. Field, L. P. Gamberg, and T. C. Rogers, Phys. Rev. **D89**, 094002 (2014), 1401.2654.
- [59] J. Collins and T. Rogers, Phys. Rev. **D91**, 074020 (2015), 1412.3820.
- [60] I. Scimemi and A. Vladimirov, JHEP **03**, 002 (2017), 1609.06047.
- [61] U. D'Alesio, M. G. Echevarria, S. Melis, and I. Scimemi, JHEP **11**, 098 (2014), 1407.3311.
- [62] M. Gluck, P. Jimenez-Delgado, and E. Reya, Eur. Phys. J. **C53**, 355 (2008), 0709.0614.
- [63] A. Buckley, J. Ferrando, S. Lloyd, K. Nordström, B. Page, M. Rüfenacht, M. Schönherr, and G. Watt, Eur. Phys. J. **C75**, 132 (2015), 1412.7420.
- [64] D. de Florian, R. Sassot, M. Epele, R. J. Hernández-Pinto, and M. Stratmann, Phys. Rev. **D91**, 014035 (2015), 1410.6027.
- [65] D. de Florian, R. Sassot, and M. Stratmann, Phys. Rev. **D75**, 114010 (2007), hep-ph/0703242.
- [66] D. de Florian, M. Epele, R. J. Hernandez-Pinto, R. Sassot, and M. Stratmann (2017), 1702.06353.
- [67] A. Bacchetta, L. P. Gamberg, G. R. Goldstein, and A. Mukherjee, Phys. Lett. **B659**, 234 (2008), 0707.3372.
- [68] B. Pasquini, S. Cazzaniga, and S. Boffi, Phys. Rev. **D78**, 034025 (2008), 0806.2298.
- [69] H. Avakian, A. V. Efremov, P. Schweitzer, and F. Yuan, Phys. Rev. **D81**, 074035 (2010), 1001.5467.
- [70] A. Bacchetta, M. Radici, F. Conti, and M. Guagnelli, Eur. Phys. J. **A45**, 373 (2010), 1003.1328.
- [71] M. Burkardt and B. Pasquini, Eur. Phys. J. **A52**, 161 (2016), 1510.02567.
- [72] A. Airapetian et al. (HERMES), Phys. Rev. **D87**, 074029 (2013), 1212.5407.
- [73] C. Adolph et al. (COMPASS), Eur. Phys. J. **C73**, 2531 (2013), [Erratum: Eur. Phys. J.C75,no.2,94(2015)], 1305.7317.
- [74] M. Anselmino, M. Boglione, J. O. Gonzalez Hernandez, S. Melis, and A. Prokudin, JHEP **04**, 005 (2014), 1312.6261.
- [75] F. Landry, R. Brock, G. Ladinsky, and C. P. Yuan, Phys. Rev. **D63**, 013004 (2001), hep-ph/9905391.
- [76] U. D'Alesio, M. G. Echevarria, S. Melis, and I. Scimemi, JHEP **11**, 098 (2014), 1407.3311.
- [77] A. S. Ito et al., Phys. Rev. **D23**, 604 (1981).
- [78] G. Moreno et al., Phys. Rev. **D43**, 2815 (1991).
- [79] T. Affolder et al. (CDF), Phys. Rev. Lett. **84**, 845 (2000), hep-ex/0001021.
- [80] B. Abbott et al. (D0), Phys. Rev. **D61**, 032004 (2000), hep-ex/9907009.
- [81] T. Aaltonen et al. (CDF), Phys. Rev. **D86**, 052010 (2012), 1207.7138.
- [82] V. M. Abazov et al. (D0), Phys. Rev. Lett. **100**, 102002 (2008), 0712.0803.
- [83] A. Abulencia et al. (CDF), J. Phys. **G34**, 2457 (2007), hep-ex/0508029.
- [84] A. Bacchetta, A. Courtoy, and M. Radici, JHEP **03**, 119 (2013), 1212.3568.
- [85] M. Radici, A. Courtoy, A. Bacchetta, and M. Guagnelli, JHEP **05**, 123 (2015), 1503.03495.
- [86] S. Forte, L. Garrido, J. I. Latorre, and A. Piccione, JHEP **05**, 062 (2002), hep-ph/0204232.
- [87] R. D. Ball, L. Del Debbio, S. Forte, A. Guffanti, J. I. Latorre, A. Piccione, J. Rojo, and M. Ubiali (NNPDF), Nucl. Phys. **B809**, 1 (2009), [Erratum: Nucl. Phys.B816,293(2009)], 0808.1231.
- [88] R. D. Ball, L. Del Debbio, S. Forte, A. Guffanti, J. I. Latorre, J. Rojo, and M. Ubiali, Nucl. Phys. **B838**, 136 (2010), 1002.4407.



- [89] M. Epele, R. Llubaroff, R. Sassot, and M. Stratmann, Phys. Rev. **D86**, 074028 (2012), 1209.3240.
- [90] S. Aid et al. (H1), Phys. Lett. **B356**, 118 (1995), hep-ex/9506012.
- [91] G. A. Ladinsky and C. P. Yuan, Phys. Rev. **D50**, R4239 (1994), hep-ph/9311341.
- [92] P. Sun, J. Isaacson, C. P. Yuan, and F. Yuan (2014), 1406.3073.
- [93] P. Schweitzer, T. Teckentrup, and A. Metz, Phys. Rev. **D81**, 094019 (2010), 1003.2190.
- [94] A. D. Martin, W. J. Stirling, R. S. Thorne, and G. Watt, Eur. Phys. J. **C63**, 189 (2009), 0901.0002.
- [95] J. F. Owens, A. Accardi, and W. Melnitchouk, Phys. Rev. **D87**, 094012 (2013), 1212.1702.
- [96] F. Hautmann, H. Jung, M. Krämer, P. J. Mulders, E. R. Nocera, T. C. Rogers, and A. Signori, Eur. Phys. J. **C74**, 3220 (2014), 1408.3015.
- [97] J. Dudek et al., Eur. Phys. J. **A48**, 187 (2012), 1208.1244.
- [98] S. J. Brodsky, F. Fleuret, C. Hadjidakis, and J. P. Lansberg, Phys. Rept. **522**, 239 (2013), 1202.6585.
- [99] M. G. Echevarria, T. Kasemets, P. J. Mulders, and C. Pisano, JHEP **07**, 158 (2015), 1502.05354.
- [100] D. Boer, S. J. Brodsky, P. J. Mulders, and C. Pisano, Phys. Rev. Lett. **106**, 132001 (2011), 1011.4225.
- [101] C. Pisano, D. Boer, S. J. Brodsky, M. G. A. Buffing, and P. J. Mulders, JHEP **10**, 024 (2013), 1307.3417.
- [102] J.-W. Qiu, M. Schlegel, and W. Vogelsang, Phys. Rev. Lett. **107**, 062001 (2011), 1103.3861.
- [103] D. Boer and C. Pisano, Phys. Rev. **D86**, 094007 (2012), 1208.3642.
- [104] W. J. den Dunnen, J. P. Lansberg, C. Pisano, and M. Schlegel, Phys. Rev. Lett. **112**, 212001 (2014), 1401.7611.
- [105] J.-P. Lansberg, C. Pisano, and M. Schlegel (2017), 1702.00305.
- [106] E. C. Aschenauer, U. D'Alesio, and F. Murgia, Eur. Phys. J. **A52**, 156 (2016), 1512.05379.
- [107] M. Boglione and A. Prokudin, Eur. Phys. J. **A52**, 154 (2016), 1511.06924.
- [108] D. Kikoła, M. G. Echevarria, C. Hadjidakis, J.-P. Lansberg, C. Lorcé, L. Massacrier, C. M. Quintans, A. Signori, and B. Trzeciak (2017), 1702.01546.